Wall-Modeled Large-Eddy Simulations for High-Lift Configurations using FUN3D

Li Wang*, W. Kyle Anderson†, Eric J. Nielsen‡, Ponnampalam Balakumar§, Michael A. Park¶, and Jan-Renee Carlson‖
NASA Langley Research Center, Hampton, VA 23681

Prahladh S. Iyer** and Boris Diskin††
National Institute of Aerospace, Hampton, VA 23666

Wall-modeled large-eddy simulation (WMLES) capability has recently been implemented into FUN3D, an unstructured, node-centered, finite-volume solver developed at the NASA Langley Research Center. In this paper, WMLES is assessed for two configurations that are representative of high-lift applications. The first configuration is a nominal two-dimensional multielement airfoil that has been extensively studied in the literature. WMLES solutions are computed for four angles of attack and compared with previously reported solutions. Good agreement of integrated forces, surface pressures, and boundary-layer velocity profiles is shown with available experimental data especially at lower angles of attack. WMLES solutions are also computed for the NASA High-Lift Common Research Model over a large range of angles of attack. Forces, pitching moments, and pressure distributions are favorably compared with the experimental data up to the maximum lift, including the angle of attack where the maximum lift is obtained experimentally. Eddy visualization techniques of q-criterion and density-gradient magnitude illustrate the resolved content.

I. Introduction

The development of improved computational capabilities for analyzing high-lift configurations is critical for commercial aircraft design, system development, and product certification [1, 2]. Over the last several decades, much of the research has been focused on developing analysis tools based on the Reynolds-averaged Navier-Stokes (RANS) models. While substantial progress has been made, as documented in Ref. [3], the ability to reliably predict aerodynamic forces and other flowfield characteristics near the maximum-lift condition is still an elusive goal.

To rectify the current situation, high-fidelity approaches that fundamentally resolve turbulent eddies are now being developed and applied for high-lift simulations. These approaches solve the unsteady three-dimensional Navier-Stokes equations that describe conservation laws for mass, momentum, and energy. The highest-fidelity approach solves the Navier-Stokes equations directly, relying on high-density grids to resolve all of the relevant physics. This method, termed direct numerical simulation (DNS), is extremely costly because turbulent flows are characterized by a vast disparity of length and time scales, ranging from the smallest Kolmogorov scales to the largest scales, which are determined by global phenomena and the configuration geometry [4, 5]. In fact, the numerical analysis of DNS has shown that the number of grid points increases as $Re^{9/4}$ and the number of time steps increases as $Re^{1/2}$ [5, 6]. As such, the required computer resources have traditionally restricted DNS to simple geometries, such as a channel or a flat plate, and moderately low Reynolds numbers.

Because of the prohibitive computational requirements for DNS, the current best practices in high-resolution simulations are to solve the Navier-Stokes equations for larger flow features and model smaller-scale flow structures. This approach, referred to as large-eddy simulation (LES), solves only for large-scale features that can be represented on a given grid and filters out small-scale effects. The latter are subsequently modeled using a subgrid-scale (SGS) model. References [6–9] describe several SGS models and their applications for incompressible and compressible flows. While

---

the LES approach is computationally more expensive than RANS, it provides significant improvements in solution accuracy. The LES methodology has been applied to a wide range of problems, but LES for wall-bounded flows at high Reynolds numbers are still prohibitively expensive due to the extremely high resolution required near the wall.

One approach, known as wall-modeled large-eddy simulation (WMLES), circumvents the high mesh-resolution requirements near the wall by modeling the inner boundary layer while accurately resolving the outer regions of the boundary layer. References [10–13] reviewed approaches that are commonly used to reduce the LES computation requirements for wall-bounded flows. There are two approaches that are predominantly used in WMLES simulations. One popular cost-reduction approach is a hybrid RANS/LES method. In this approach, the inner boundary layer is solved using a RANS turbulence model and LES is applied in the rest of the domain [11, 12]. The second method, known as a wall-stress modeling approach, uses underlying RANS assumptions to extract the wall shear stress, and applies it as a boundary condition for LES that is conducted down to the wall [14–18]. This shear-stress modeling approach is used in the present work.

For high-lift applications, the WMLES approach is increasingly being adopted in the research community for simulating nominally two-dimensional multielement airfoils [19–21] and fully three-dimensional aircraft configurations [21–24]. To enhance the capabilities for computing high-lift configurations, and to provide a platform for further research, a WMLES capability has recently been implemented in FUN3D, an unstructured, node-centered, finite-volume solver developed at the NASA Langley Research Center. The present study evaluates the initial implementation of the WMLES capability for high-lift configurations. Specifically, nominally two-dimensional simulations are conducted for the McDonnell Douglas 30P30N airfoil. The solutions are validated using the experimental data obtained during a cooperative campaign that involved Douglas Aircraft Company and the NASA Langley Research Center [25, 26]. Another set of simulations is performed on the NASA High-Lift Common Research Model (CRM-HL) [27]. Forces, moments, and pressure distributions are evaluated for a large range of angles of attack, including the angle of attack corresponding to the maximum-lift condition.

The rest of the material in the paper is presented in the following order. Section II describes the governing equations. Section III outlines the discretization scheme and iterative solvers available in FUN3D for WMLES computations. Numerical results for flows over the McDonnell Douglas 30P30N multielement airfoil and the NASA CRM-HL configuration are presented and discussed in Section IV, where comparisons of the WMLES solutions are made with available experimental data. Finally, Section V offers conclusions and directions of future work.

II. Governing Equations

The governing equations are the compressible, spatially-filtered Navier-Stokes equations, which can be expressed in the following conservative form:

$$\frac{\partial \mathbf{Q}(\mathbf{x}, t)}{\partial t} + \nabla \cdot (\mathbf{F}_e(\mathbf{Q}) - \mathbf{F}_v(\mathbf{Q}, \nabla \mathbf{Q})) = 0 \quad \text{in } \Omega \tag{1}$$

where Ω is a bounded domain. The vector of conservative flow variables, $\mathbf{Q}$, and the inviscid and viscous Cartesian flux vectors, $\mathbf{F}_e$ and $\mathbf{F}_v$, are defined as follows,

$$\mathbf{Q} = \begin{bmatrix} \rho \\ \rho u \\ \rho v \\ \rho w \\ \rho E \end{bmatrix}, \quad \mathbf{F}_e^x = \begin{bmatrix} \rho u \\ \rho u^2 + p \\ \rho uv \\ \rho uw \\ (\rho E + p)u \end{bmatrix}, \quad \mathbf{F}_e^y = \begin{bmatrix} \rho v \\ \rho uv \\ \rho v^2 + p \\ \rho vw \\ (\rho E + p)v \end{bmatrix}, \quad \mathbf{F}_e^z = \begin{bmatrix} \rho w \\ \rho uw \\ \rho vw \\ \rho w^2 + p \\ (\rho E + p)w \end{bmatrix}, \tag{2}$$

$$\mathbf{F}_v^x = \begin{bmatrix} 0 \\ \tau_{xx} \\ \tau_{xy} \\ \tau_{xz} \\ u\tau_{xx} + v\tau_{xy} + w\tau_{xz} + \kappa\frac{\partial T}{\partial x} \end{bmatrix}, \quad \mathbf{F}_v^y = \begin{bmatrix} 0 \\ \tau_{xy} \\ \tau_{yy} \\ \tau_{yz} \\ u\tau_{xy} + v\tau_{yy} + w\tau_{yz} + \kappa\frac{\partial T}{\partial y} \end{bmatrix},$$

$$\mathbf{F}_v^z = \begin{bmatrix} 0 \\ \tau_{xz} \\ \tau_{yz} \\ \tau_{zz} \\ u\tau_{xz} + v\tau_{yz} + w\tau_{zz} + \kappa\frac{\partial T}{\partial z} \end{bmatrix}. \tag{3}$$

Here, ρ, p, and E denote the fluid density, pressure, and specific total energy per unit mass, respectively, and $\mathbf{u} = (u, v, w)$ represents components of the Cartesian velocity vector. The pressure p is determined by the equation of state for an ideal gas,

$$p = (\gamma - 1)\left(\rho E - \frac{1}{2}\rho(u^2 + v^2 + w^2)\right), \tag{4}$$

where γ is the ratio of specific heats, $\gamma = 1.4$ for air. Note that all the flow quantities here represent filtered (or resolved) variables. The τ subscripts represent the components of the total (viscous and turbulent) stress tensor, which for a Newtonian fluid are defined as,

$$\tau_{ij} = (\mu + \mu_T)\left(\frac{\partial \mathbf{u}_i}{\partial \mathbf{x}_j} + \frac{\partial \mathbf{u}_j}{\partial \mathbf{x}_i} - \frac{2}{3}\frac{\partial \mathbf{u}_k}{\partial \mathbf{x}_k}\delta_{ij}\right). \tag{5}$$

Here, δ_{ij} is the Kronecker delta operator and subscripts i, j, k refer to the Cartesian coordinates $\mathbf{x} = (x, y, z)$. The notations κ and T denote the total thermal conductivity and temperature, respectively, and satisfy the following relation:

$$\kappa T = \gamma\left(\frac{\mu}{Pr} + \frac{\mu_T}{Pr_T}\right)\left(E - \frac{1}{2}\left(u^2 + v^2 + w^2\right)\right). \tag{6}$$

In Eqs. (5) and (6), μ refers to the dynamic viscosity, which is obtained via Sutherland's law[28], and μ_T denotes the modeled SGS viscosity; Pr and Pr_T are the meanflow Prandtl number and the turbulent Prandtl number that are set to be 0.72 and 0.9, respectively. In the present work, μ_T is obtained using the model presented in Ref. [29], which is summarized below:

$$\mu_T = \rho C\sqrt{\frac{B_\beta}{\alpha_{ij}\alpha_{ij}}}, \tag{7}$$

where

$$\alpha_{ij} = \frac{\partial u_j}{\partial x_i}, \tag{8}$$

$$\beta_{ij} = \Delta_m^2 \alpha_{mi}\alpha_{mj}, \tag{9}$$

$$B_\beta = \beta_{11}\beta_{22} - \beta_{12}^2 + \beta_{11}\beta_{33} - \beta_{13}^2 + \beta_{22}\beta_{33} - \beta_{23}^2. \tag{10}$$

The modeling constant, C, used in the present study is the one suggested in Ref. [29], which is related to the Smagorinsky constant as follows, $C \approx 2.5C_s^2$ and $C_s = 0.17$. The local filter width, Δ_m ($m = 1, 2$, and 3), is currently set to be the cube root of the cell volume, considering the use of nearly isotropic grids. Future research on adjusting this parameter to account for grid anisotropy can be performed. It is also noted that turning off the SGS model described above reduces the model to an implicit LES model, which uses the nonlinear truncation error of the discretization scheme for the Navier-Stokes equations to provide SGS closure [9]. However, the use of explicit versus implicit LES in conjunction with the wall-stress model is out of the scope of the current presentation.

III. Solution Algorithm

FUN3D [30, 31] solves the governing equations discretized on unstructured, mixed-element grids. The grids may contain tetrahedra, pyramids, prisms, and hexahedra. Median-dual control volumes are constructed around grid points. Inviscid fluxes are computed at edge medians by using an approximate Riemann solver. In the current study, Roe's flux-difference splitting [32] is used. For second-order accuracy, density, pressure, and velocity at edge medians are reconstructed by an unstructured monotonic upstream scheme for conservation laws (UMUSCL) [33, 34]. For mixed-element grids, the UMUSCL parameter is initiated as $\kappa_u = 0.5$ and subsequently increases to $\kappa_u = 0.9$ in later stages of the solution process to reduce dissipation; $\kappa_u = 0.5$ is maintained on solid surfaces. Note that as the κ_u parameter approaches unity, the scheme tends toward central differencing. For discretization of the viscous fluxes, the Green-Gauss theorem is used to compute cell-based gradients. In the case of tetrahedral grids, this approach is equivalent to a Galerkin-type approximation. For nontetrahedral grids, cell-based Green-Gauss gradients are combined with edge-based gradients to improve stability of viscous operators and prevent odd-even decoupling. Specifically, an edge-normal augmentation scheme [35] is used. The viscous fluxes are second-order accurate on general mixed-element grids [36, 37] including transition regions with different element types.

The boundary conditions used in the present study include a farfield Riemann solver, symmetry plane, and viscous-wall boundary conditions. At the farfield, the boundary conditions are weakly enforced by constructing an exterior state based on the freestream conditions to close the boundary fluxes. The symmetry boundary conditions strongly enforce zero normal velocity at the boundary grid points, while the tangential momentum, mass, and energy conservation at the symmetry plane are enforced weakly through the conservation equations. The WMLES implementation largely follows the methodology described in Ref. [14]. At each time step, flowfield variables are extracted at predetermined exchange locations, which are the first points off the wall in the present work. The extracted solutions serve as input to a simple equilibrium wall model [38], which is used to determine the local shear stress at each grid point on the solid-wall surface. Once the shear stress is determined, it is used to compute boundary-face fluxes required for evaluating the residuals at the boundary grid points.

An implementation of wall functions for RANS simulations has been previously reported in Ref. [39]. The implementation in the current work is similar with some modifications. The nonlinear equation [38] that is solved to compute shear stress is fully linearized in the current implementation. The geometry-related terms near boundaries are modified to improve accuracy, as described in Ref. [40].

The solution at each time step is obtained using a second-order accurate implicit time-stepping scheme [41]. At each time step, the discrete nonlinear system of equations can be expressed as:

$$\mathbf{R}(\mathbf{Q}) = \mathbf{0}, \tag{11}$$

where $\mathbf{Q}$ denotes the flow solution and $\mathbf{R}$ denotes the nonlinear unsteady residual. This nonlinear system of equations at each time step is solved by an approximate Newton-type method with a pseudotime term expressed as:

$$\left[\frac{V}{\Delta\tau}\mathbf{I} + \widetilde{\frac{\partial\mathbf{R}}{\partial\mathbf{Q}}} \right] \Delta\mathbf{Q} = -\mathbf{R}(\mathbf{Q}^n), \tag{12}$$

$$\mathbf{Q}^{n+1} = \mathbf{Q}^n + \omega\,\Delta\mathbf{Q}. \tag{13}$$

Here, V is a dual-cell volume; $\Delta\tau$ is the local pseudotime step governed by the Courant-Fredrichs-Lewy (CFL) number; $\mathbf{I}$ is the identity matrix; the superscript n is the nonlinear iteration index, and ω is an under-relaxation parameter. Note that because $\mathbf{R}(\mathbf{Q})$ represents the unsteady residual, the physical time derivative is included in Eq. (11), although it is not explicitly shown. The approximate linearization, $[\partial\mathbf{R}/\partial\mathbf{Q}]$ in Eq. (12), also includes the contributions from the time derivatives.

Two nonlinear solution methods are available in FUN3D: a simple defect-correction solver and a strong nonlinear iteration solver. The defect-correction method solves the linear system shown in Eq. (12) with point-implicit Gauss-Seidel (GS) iterations together with linear CFL ramping. The strong nonlinear solver, referred to as a hierarchical adaptive nonlinear iteration method (HANIM), uses additional hierarchies including a matrix-free Newton-Krylov scheme for the linear system and an adaptive CFL strategy to improve robustness and efficiency. More details of the solution methods can be found in Ref. [42]. Specification of solver parameters is given in Section IV for each test case.

IV. Numerical Results

In this section, WMLES solutions are assessed for flows over high-lift configurations, including the McDonnell Douglas 30P30N multielement airfoil and the NASA CRM-HL aircraft model. A large range of angles of attack are considered in each test example to evaluate the model capability for maximum-lift ($C_{L,max}$) predictions. Simulation results are systematically compared to experimental data.

A. McDonnell Douglas 30P30N Multielement Airfoil

WMLES for flow past the McDonnell Douglas 30P30N multielement airfoil [26] are presented at several flow conditions specified at the AIAA 4th High Lift Prediction Workshop webpage [43]. This same configuration, and many of the same flow conditions, have previously been used for assessing RANS and LES models for computing high-lift flows [19–21, 44]. In this work, the following flow conditions are used. The freestream Mach number is 0.2 and the Reynolds number, based on the chord of the airfoil in the undeflected position, is 9 million. The angles of attack are $\alpha = 8.10°, 16.21°, 21.34°$ and $23.28°$.

The configuration is a nominally two-dimensional airfoil extruded in the spanwise direction. The spanwise extent of the computational domain is $0.04c$, where c is the chord length of the airfoil in the undeflected position. This extent is small and may hinder the resolution of some three-dimensional effects between the side-wall planes. Simulations have been performed on two grids: a coarse grid with approximately 2.9 million points and a fine grid with approximately 10 million points. These grids are unstructured on the plane of the airfoil, although they are mostly composed of hexahedra. The coarse grid has 2.74 million hexahedra and 110 thousand prisms, and the fine grid has 9.68 million hexahedra and 308 thousand prisms.
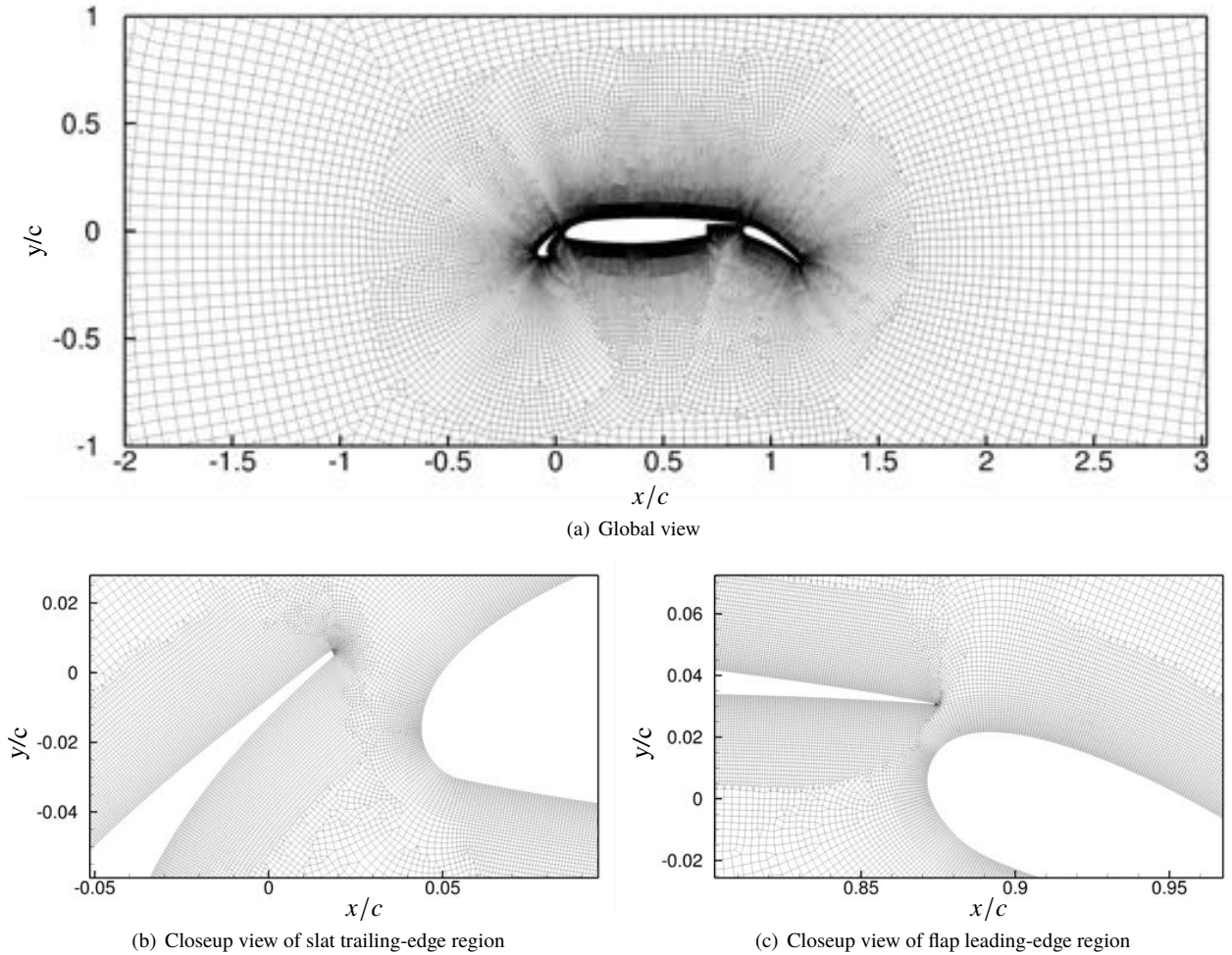
The computational domain extends to $100c$ within the plane of the airfoil where farfield boundary conditions are imposed. Periodic boundary conditions are applied on the side planes. For the fine grid, there are 44 parallel computational planes uniformly spaced in the spanwise direction. The spacing between the planes is approximately $0.0009c$. The airfoil surface mesh is clustered near the leading and trailing edges. The streamwise surface spacing is approximately $0.0009c$, except in the immediate vicinity of the leading and trailing edges of the airfoil, where this spacing is finer by a factor of 5. The minimum of the wall-normal spacing is $0.00033c$ (targeting a nominal $\Delta y_w^+ \approx 100$ based on a flat-plate approximation at the freestream condition and the reference length c) with a growth rate of 1.05 for 25 grid layers. Because the boundary-layer thickness at $x/c = 0.85$ is approximately $0.015c$ for $\alpha = 8.10°$, the fine grid contains roughly 16 points within the boundary layer at this location. Compared to the fine grid, the coarse grid has a similar wall-normal spacing but is coarser by a factor of 2 in each direction within the airfoil plane. The spacing between planes is two times coarser for the coarser grid.

Several views of the fine grid are shown in Fig. 1. Closeup views are shown between the slat and the leading edge of the main element and between the flap and the trailing edge of the main element in Figs. 1(b) and 1(c), respectively. Views of the surface mesh and periodic side-wall mesh are shown in Fig. 2. Figure 2(a) shows the surface mesh of the slat. Figure 2(b) shows the mesh at the trailing edge of the main element and the leading edge of the flap. The ratio of streamwise to spanwise spacing of the surface elements is close to unity over the majority of the surface.

On the fine mesh, the simulations are conducted with a time step so that 1,111 time steps represent a single convective time unit (CTU). Here, CTU is defined as the time unit for flow passing through the main characteristic length based on the freestream velocity, i.e., CTU = c/U_∞. The coarse-grid simulations use a twice larger time step. About 140 CTUs are performed with a dozen times larger time step than the nominal one to eliminate transients. Simulations are then conducted over 50 CTUs with the nominal time step until the forces stabilized, after which statistics were taken for additional 30 CTUs. The standard second-order backward difference formula (BDF2) is employed in these simulations. The defect-correction solver is used with 5 subiterations and 20 linear GS sweeps per subiteration. The residuals are reduced by at least a factor of 8 at each time step. The solution reconstruction is switched to first order when a Ducros sensor [45] identifies shocks in the flow. The simulations are conducted without an explicit subgrid-scale model, which effectively reduces to implicit LES.

Figure 3 depicts the variation of lift with angle of attack on the coarse and fine grids and compares it with experimental data by Klausmeyer and Lin [44]. At $\alpha = 8.10°$, the coarse-grid solution significantly overpredicts lift compared to the experimental data, whereas lift computed on the fine grid is within 1% of the experimental value. Similarly, at $\alpha = 16.21°$, lift is captured well by the fine grid while lift on the coarse grid is overpredicted. At the higher angles of attack, namely $\alpha = 21.34°$ and $\alpha = 23.28°$, the solutions obtained on both grids underpredict the experimental lift value by 3–4%, although both solutions appear to qualitatively capture the stall. However, Ref. [46] reports that, above $\alpha = 16°$, noticeable spanwise pressure variations are observed on the flap in the experiment, which indicates

(a) Global view

(b) Closeup view of slat trailing-edge region

(c) Closeup view of flap leading-edge region

Fig. 1   Views of the fine grid used for the 30P30N simulations.

three-dimensional effects that are not modeled in the present simulations. Similar comments regarding the experimental data can be found in Ref. [26], which includes experimental spanwise pressure distributions along the trailing edges of the elements, and Ref. [47], which shows experimentally obtained pressure distributions at several spanwise stations at $\alpha = 16.20°$, $\alpha = 21.31°$, and $\alpha = 22.25°$.

Figure 4 compares the time-averaged pressure coefficients computed on the fine grid with the experimental data for the four angles of attack considered in this study. At $\alpha = 8.10°$, the WMLES computation slightly overpredicts the pressure at the suction side of the slat. The agreement is good over the main element and flap. At $\alpha = 16.21°$, the agreement is good over all the sections of the airfoil. For the two higher angles of attack, mild underprediction is observed over the main element and flap, probably caused by three-dimensional effects; agreement is slightly better for $\alpha = 21.34°$ than for $\alpha = 23.28°$.

Instantaneous velocity magnitude contours computed on the fine grid are shown in Fig. 5 for the four angles of attack on the fine mesh. Unsteadiness of the wake emanating from the slat is captured in the simulations. As the angle of attack is increased, the low-momentum fluid above the flap becomes more pronounced. It appears that the flow between the main element wake and flap shear layer becomes increasingly unsteady as stall is approached at $\alpha = 21.34$ and $23.28°$.

Figures 6 and 7 compare time-averaged profiles of velocity magnitude computed on the fine grid with the experiment. The comparisons are reported for four stations and $\alpha = 8.10°$ and $\alpha = 16.21°$. The notation d_n in the plots denotes the wall distance. The $x/c = 0.45$ station is located approximately midchord on the main element. The positions of the other stations can be determined by cross referencing the profile locations shown in Fig. 8. Note that in this figure,

6

(a) Surface mesh near slat and main element

(b) Surface mesh near main element and flap
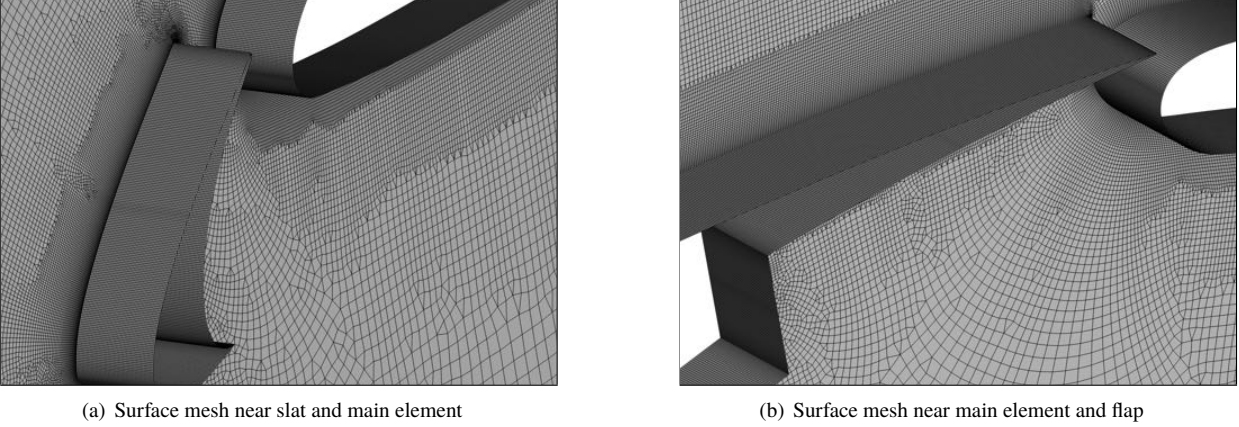
Fig. 2   Surface mesh for the 30P30N airfoil.
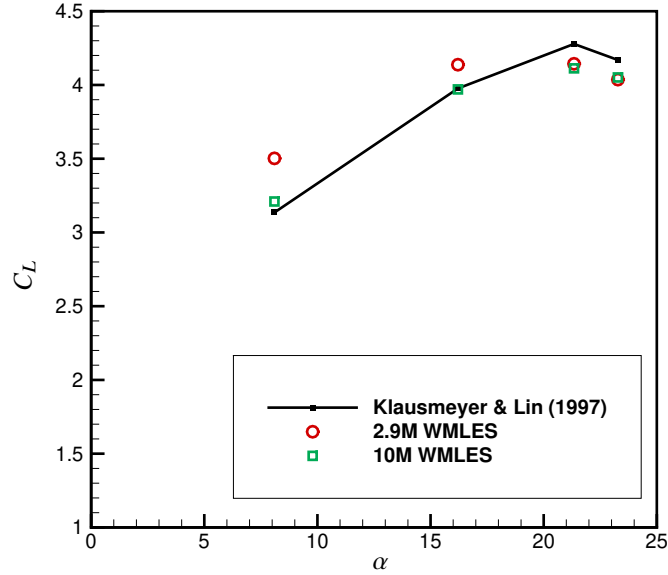

**Fig. 3   Variation of lift with angle of attack for the 30P30N airfoil.**

the station locations ($x/c = 0.85$, $x/c = 0.8982$, $x/c = 0.9750$, $x/c = 1.0321$, $x/c = 1.0752$, and $x/c = 1.1125$) are ordered from upstream to downstream; the indicated coordinates are relative to the airfoil in the undeflected position. Fair overall agreement is observed between the WMLES computations and experiment. Some of the discrepancy may be caused by laminar-turbulent transition present in the experiment, which is not accounted for in the WMLES simulations. Also, the thin boundary layer closer to the leading edge of the main element appears to be insufficiently resolved. At $\alpha = 16.21°$, the slat wake is more prominent in the experimental data than in the computations, particularly at the further downstream stations. Note that the circles shown in Fig. 8 indicate the approximate location of the center of the slat wake, as extracted from the experimental data at $\alpha = 16.21°$. As seen in Fig. 8, the mesh lacks sufficient resolution away from the immediate vicinity of the wall. The slat wake is not accurately resolved in the computations and is therefore more diffused compared to the experiment. An adaptive mesh refinement technique is of great interest to provide necessary grid resolution.
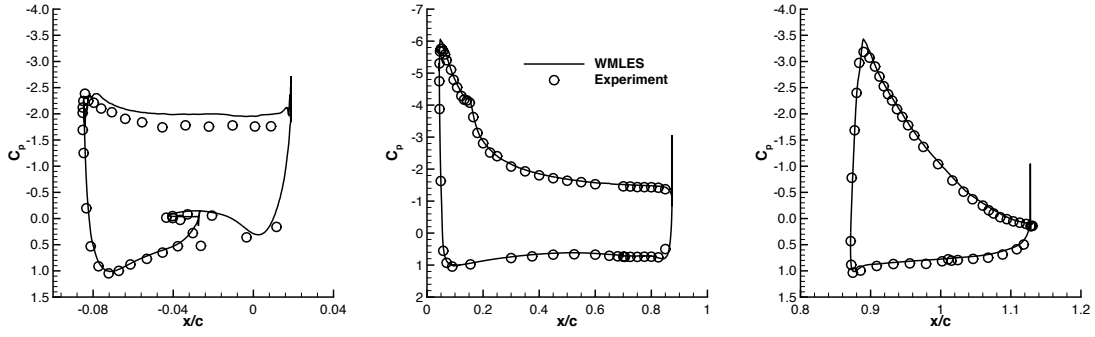
(a) $\alpha = 8.10°$
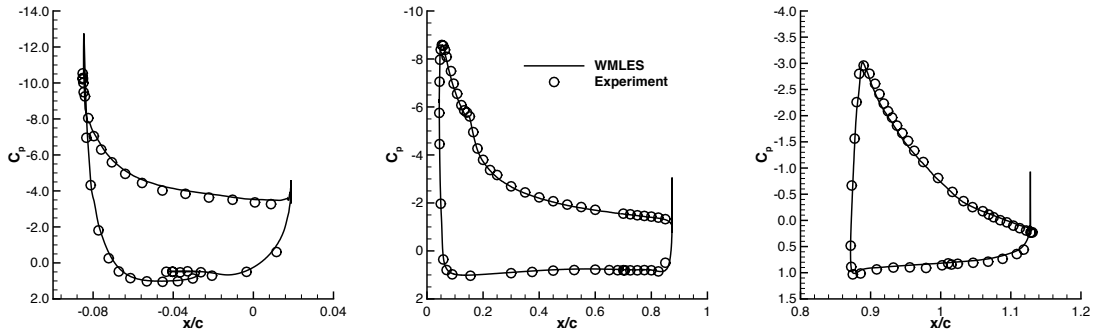
(b) $\alpha = 16.21°$
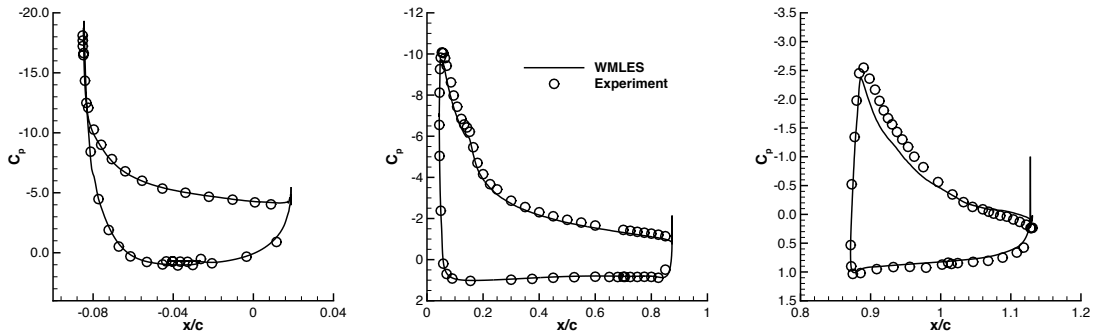
(c) $\alpha = 21.34°$
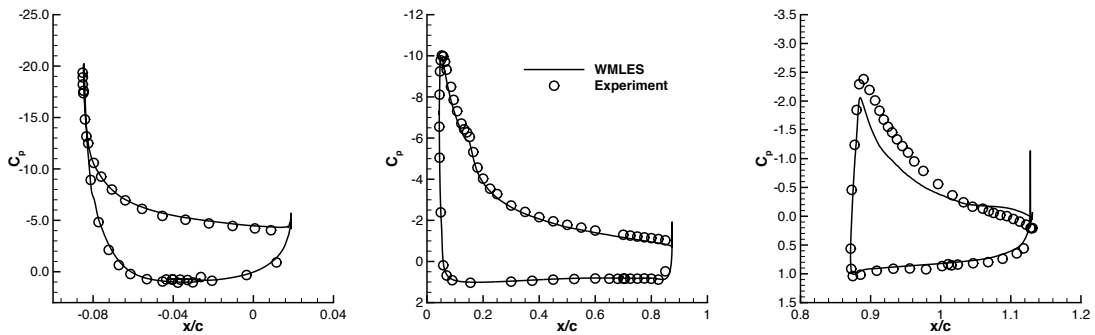
(d) $\alpha = 23.28°$

Fig. 4 Pressure distribution for 30P30N configuration on fine grid: $M_\infty = 0.3$, $R_e = 9.0 \times 10^6$.
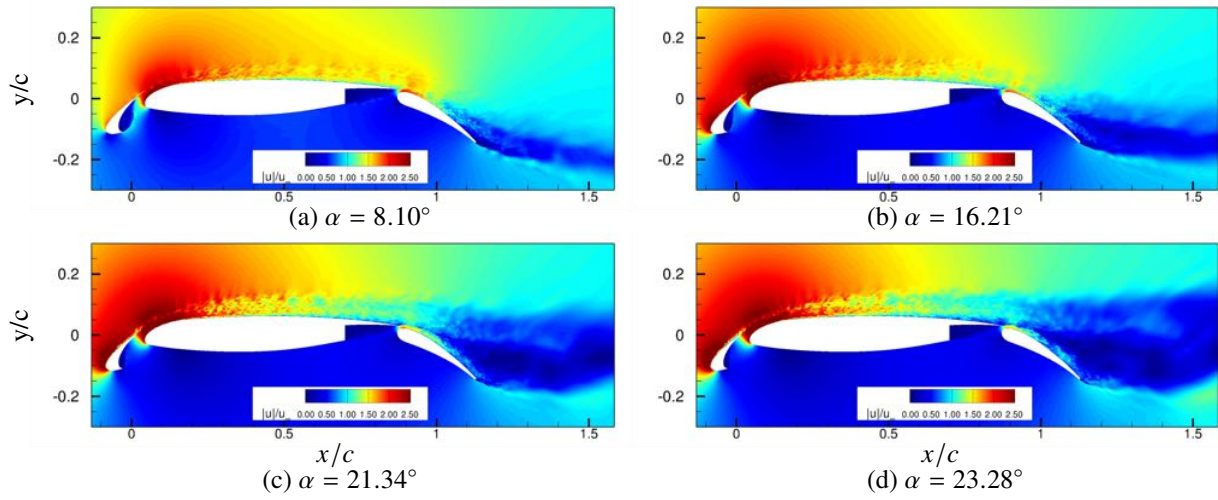
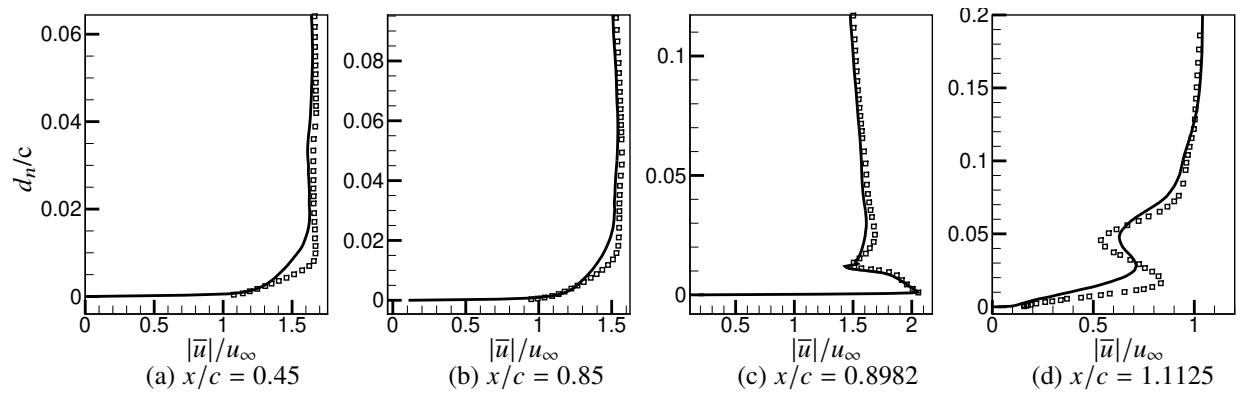**Fig. 5 Instantaneous velocity magnitude contours for the 30P30N simulations on fine grid.**

Fig. 6 Time-averaged velocity magnitude for WMLES (solid line) and experiment (symbols) for 30P30N at $\alpha = 8.10°$.
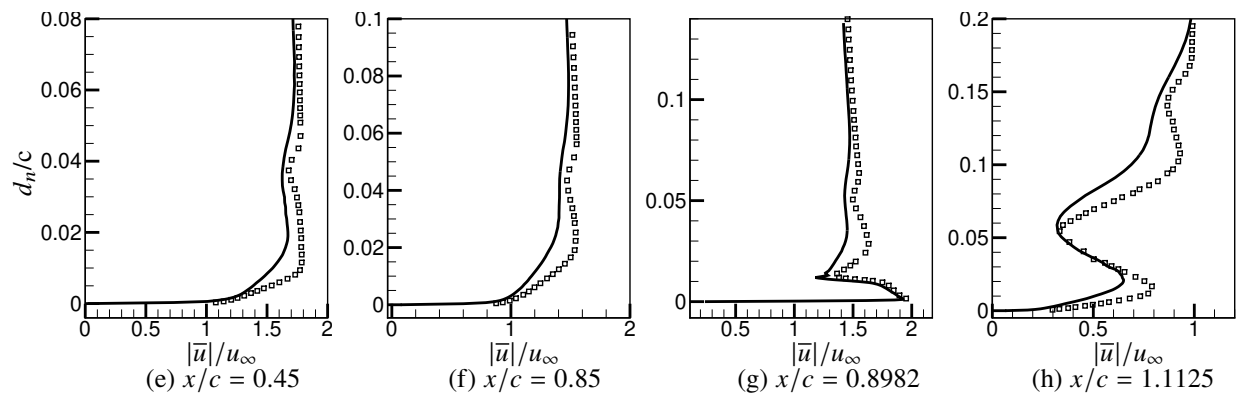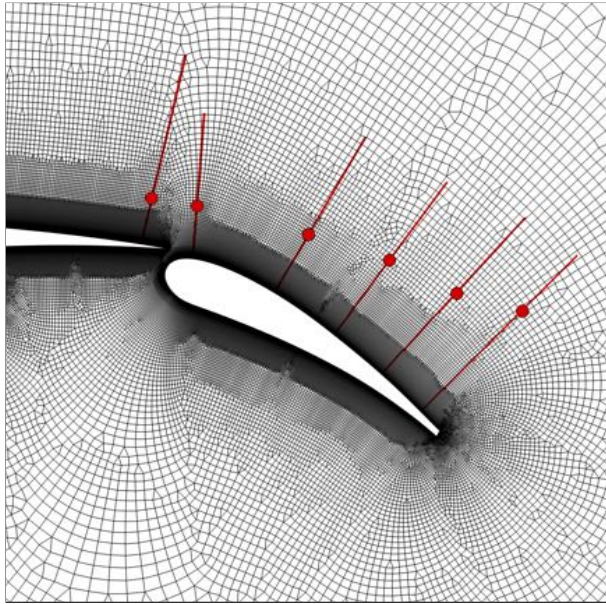

Fig. 7 Time-averaged velocity magnitude for WMLES (solid line) and experiment (symbols) for 30P30N at $\alpha = 16.21°$.

Fig. 8   Approximate slat-wake location for 30P30N airfoil at $\alpha = 16.21°$**.**

B. NASA High-Lift Common Research Model

In this section, WMLES are presented for flows over the NASA CRM-HL model at a range of angles of attack, with the flaps in a landing configuration. The NASA CRM-HL configuration is a 10%-scale, semispan model that was tested in the QinetiQ 5-meter pressurized low-speed wind tunnel [27]. The experimental data are used for evaluating CFD simulations as part of the 4th AIAA CFD High Lift Prediction Workshop [43].

1. Configuration and Flow Conditions

The NASA CRM-HL geometry incorporates many salient features of a realistic flight configuration, including a fuselage, a flow-through nacelle, nacelle pylon, nacelle chine, leading-edge slats, slat brackets, a main wing, trailing-edge flaps, and flap fairings. Experimental data have been obtained for three combinations of inboard/outboard trailing-edge flap deflections ($37°/34°$, $40°/37°$, and $43°/40°$), all with $30°$ deflection of a partial-span leading-edge slat. Landing gear and horizontal or vertical tails are not included in the current configuration. Experimental data for lift, drag, pitching moment about the spanwise axis, surface pressures, and oil-flow visualizations were obtained at different angles of attack, including $\alpha = 2.78°$, $7.05°$, $11.29°$, $17.05°$, $19.57°$, $20.55°$, and $21.47°$ (wall corrected).

In this work, free-air simulations are conducted for the nominal trailing-edge flap deflections of $40°/37°$. The flow conditions for this configuration are a freestream Mach number of 0.2, a Reynolds number of 5.49 million based on the mean aerodynamic chord (MAC) of 275.8" and a reference temperature of 521 °R. This case corresponds to Case 2a of the workshop. More details about the geometry, test parameters, and related references are available from the workshop website [43]. Figure 9 displays the locations of spanwise slices (A–H) where experimental data are available for CFD validation; slices highlighted in red (i.e., A, D, E, and G) are stations used in this paper.
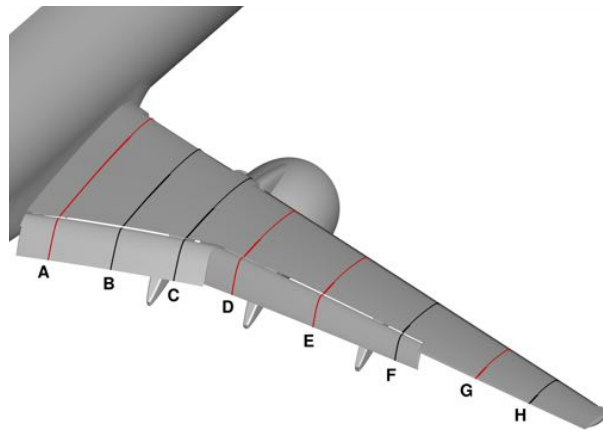

Fig. 9   Slice locations for NASA CRM-HL experimental data.

2. Grids

Two unstructured grids, referred to as Mesh A and Mesh B, are used to assess the WMLES performed for the full angle-of-attack range. These grids also serve as a control group in a preliminary grid-sensitivity study in which a third grid, referred to as Mesh C, is generated; Mesh C is similar in size to Mesh B, but has a larger normal spacing at the wall. As discussed later in Section IV.B.3, the increased wall-normal spacing for Mesh C is likely to place the first point off the wall outside the log-law region of the boundary layer. Since the first points off the wall are used in the present work as the exchange locations, questions are raised about the adequacy of the simple wall model [38] that is valid only from the wall to the outer edge of the log-law region. Consequently, simulations on Mesh C are limited to a subset of the cases to examine the wall-spacing effects on the simulations.

For all of the computational grids, the symmetry plane is located at $y = 0$. The outer boundary is located about 100 MAC lengths away. Mesh A and Mesh B contain approximately 418 million and 156 million grid points, respectively.

Although generated independently, both grids have a nominal wall-normal spacing of 0.13", corresponding to a nominal $\Delta y_w^+ \approx 100$ based on a flat-plate approximation at freestream conditions and the MAC reference length. Along the surfaces of the slat, main wing, and flap, the grid points away from the leading and trailing edges are uniformly distributed. In the vicinity of the leading and trailing edges, clustering is used to improve accuracy in regions with large solution gradients. Mesh C is isotropic with 0.5" spacing in all directions and does not have clustering at the leading and trailing edges. The surface normal spacing corresponds to $\Delta y_w^+ \approx 385$. More details about the grid metrics are provided in Table 1.

Figure 10 displays slices of Mesh A and Mesh B at Station D that are representative of slices at the other stations. These figures provide views of the overall grid topologies, as well as point distributions near the surfaces of the main-wing cove and flap. Mesh A is constructed using a layered approach, where the elements in each layer are roughly twice larger than the elements in the neighboring layer closer to the surface. In the regions between the layers, tetrahedral and pyramidal elements are used to blend the layers. Mesh B uses mostly prisms for the boundary-layer cells and mostly tetrahedra away from the surface. Mesh A achieves somewhat higher density than Mesh B above the main element and flap. It is expected that the higher density above the main element and flap should provide somewhat better resolution of the slat and main-element wakes.

A view of the entire surface mesh is not informative because the density of grid points is so high that no useful information can be visualized. Representative closeup views of the surface mesh in the vicinity of the fuselage are shown in Fig. 11. Figure 11(a) shows a closeup view of the surface of Mesh A, in the vicinity of the fuselage as indicated in Fig. 11(c). Figure 11(b) is the view of Mesh B in the same region. Both grids have fine surface resolution. The ratio of streamwise to spanwise spacing on the surface elements of Mesh A is approximately two. This ratio for Mesh B is nominally unity away from the leading and trailing edges. Near the leading and trailing edges, however, Mesh B has somewhat higher density and this ratio remains approximately unity despite clustering.

3. Simulation Results

Five angles of attack, namely $\alpha = 7.05°$, $17.05°$, $19.57°$, $20.55°$, and $21.47°$, are considered for WMLES using both Mesh A and Mesh B. The WMLES computations for $\alpha = 11.29°$ case are conducted on Mesh A to provide additional assessments.
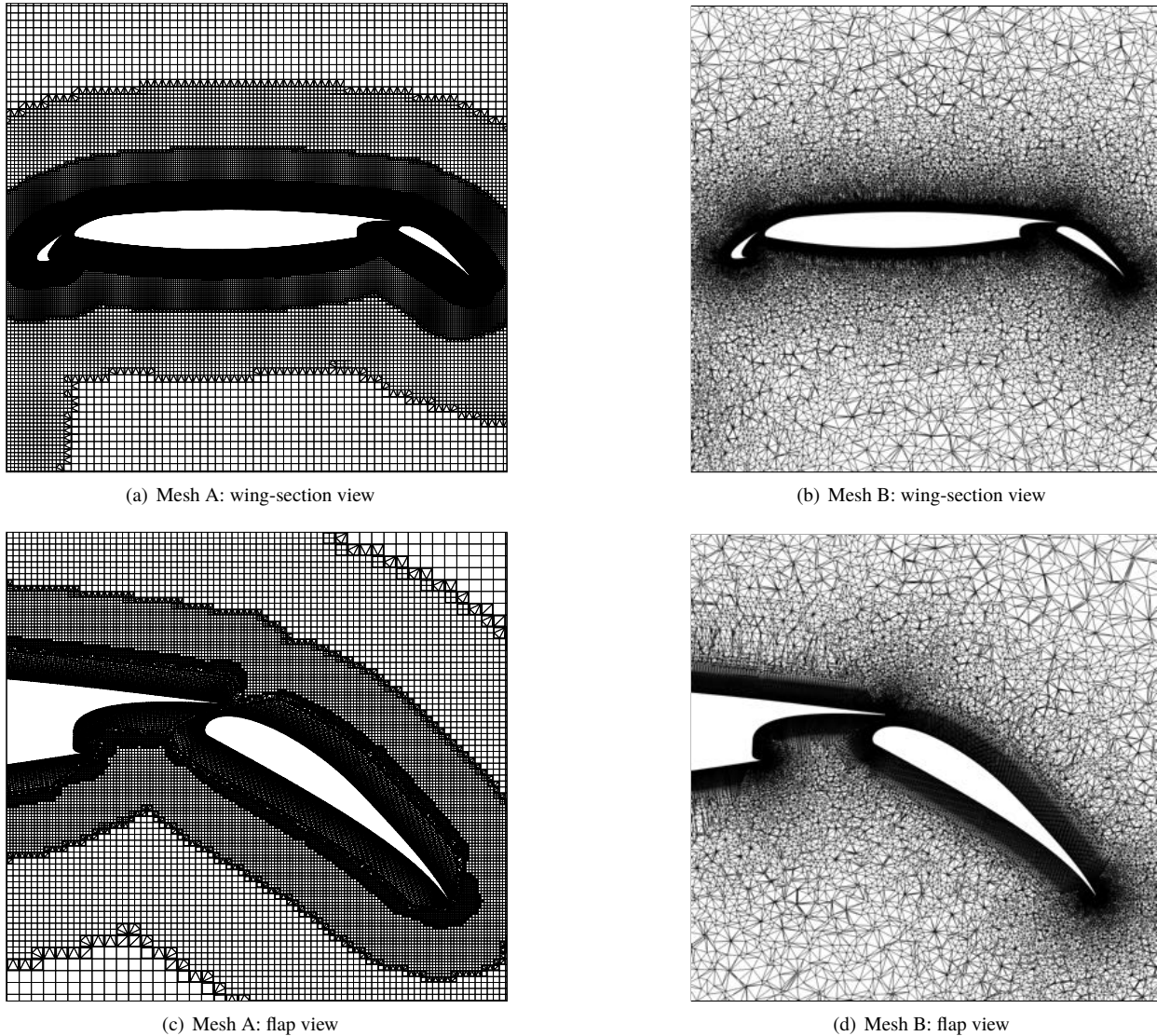
The initial time step is chosen so that 1,000 time steps represent a single CTU and the first 8–10 CTUs are used to eliminate initial transients. Afterward, the time step is reduced to achieve 2,000 time steps per CTU to improve the temporal accuracy. The UMUSCL parameter for inviscid fluxes is initially set to $\kappa_u = 0.5$, and increased to $\kappa_u = 0.9$ after 4-5 CTUs to reduce the spatial dissipation. Time-averaged quantities such as density, velocity components, and pressure are collected over 5–15 CTUs after the transients in the forces and moments have been reduced.

The implicit system of equations is solved using HANIM, described in Ref. [42]. In HANIM, the CFL number, which controls the pseudotime stepping, is adapted based on the performance of various HANIM modules. In the present simulations, the operational range of CFL number is between 1.0 and 1,000 at each time step with 6–8 subiterations, resulting in 4–5 orders of magnitude in residual reduction.

Table 1 NASA CRM-HL Mesh Statistics.

Ordering	Mesh A	Mesh B	Mesh C
Nodes	418, 774, 938	156, 117, 308	142, 708, 069
Tetrahedrons	396, 153, 823	245, 076, 460	193, 686, 407
Pyramids	97, 054, 752	14, 799, 748	60, 003, 831
Prisms	1, 787, 526	215, 323, 499	1, 099, 421
Hexahedrons	317, 281, 293	0	87, 029, 789
Surface points	7, 418, 554	5, 011, 436	6, 992, 786
Surface triangles	176, 232	9, 746, 096	0
Surface quadralaterals	7, 892, 108	168, 929	7, 076, 671
Nominal Δy_w^+	100	100	385

(a) Mesh A: wing-section view

(b) Mesh B: wing-section view

(c) Mesh A: flap view

(d) Mesh B: flap view

Fig. 10 NASA CRM-HL mesh slices at Station D.

Time histories of the integrated lift, drag, and pitching-moment coefficients computed on Mesh A are shown in Fig. 12 as a function of CTU for the $\alpha = 7.05°$, $19.57°$, and $21.47°$. Although not shown, other angle-of-attack cases exhibit similar convergence behavior. For higher angles of attack, WMLES require more flow-through passes to reach statistically stationary states, especially to attain the pitching-moment convergence. A longer integration time is needed at higher pitch angles because of increased complexity of high-lift flows that exhibit flow separation and interactions of turbulent boundary layers with wakes. All WMLES computations in this work have been performed with sufficiently long integration time to attain reasonably converged solutions, although longer time averaging may be required to fully smooth out oscillations present in the pressure distributions (discussed later in this section).

Figure 13 compares integrated forces and moments computed by free-air WMLES on Mesh A and Mesh B with the wall-corrected experimental measurements. Computed lift coefficients are shown in Fig. 13(a) versus the angle of attack. For the $\alpha = 7.05°$ case, the lift coefficients predicted on Mesh A and Mesh B show good agreement with each other and the experimental data. At $\alpha = 11.29°$, where the lift curve is approximately linear, WMLES computations on Mesh A continue to exhibit good agreement with the experiment; WMLES on Mesh B have not been performed at this angle of attack. The lift coefficient computed on Mesh A at $\alpha = 17.05°$ is slightly below that of the experimental data, whereas the lift coefficient computed on Mesh B is slightly above the experiment. Both the computed lift coefficients

(a) Mesh A   (b) Mesh B   (c) Location on surface for closeup view
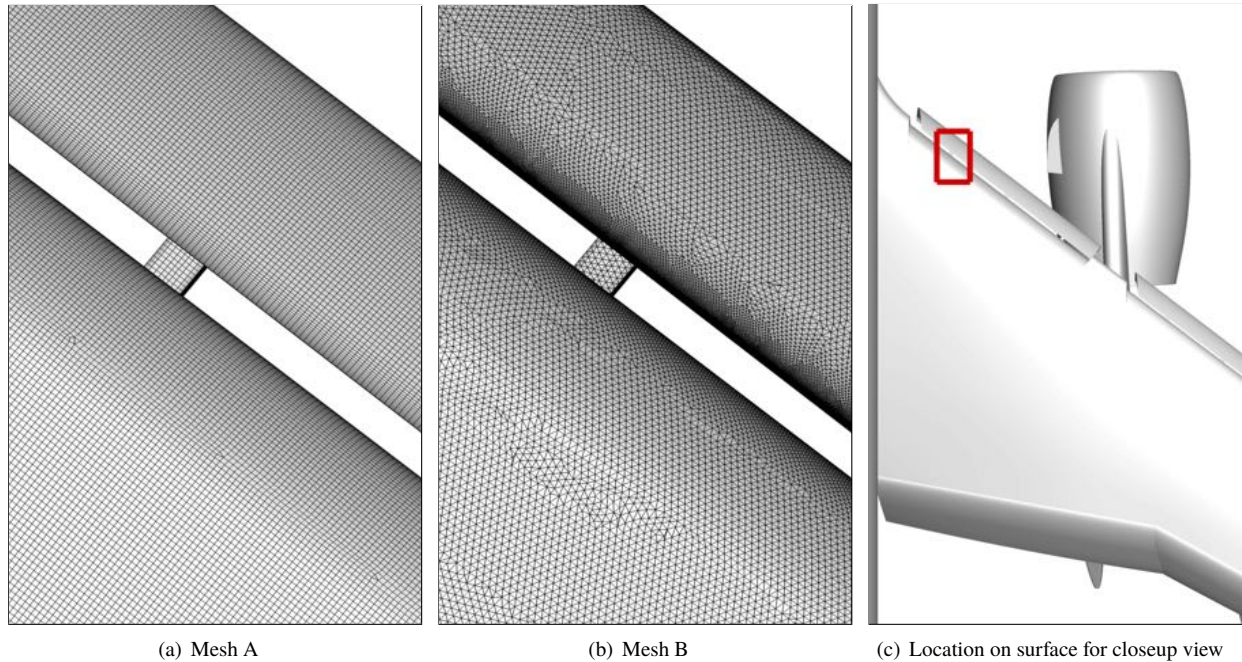
Fig. 11   NASA CRM-HL surface mesh near fuselage.

continue to match the experimental data well, showing approximately 2–3% deviation from the measurement. At $\alpha = 19.57°$ corresponding to the experimental $C_{L,max}$, WMLES computations on Mesh A accurately predict the critical angle of attack for $C_{L,max}$, and the difference in the lift coefficient is within 1%. The Mesh-B WMLES computations slightly underpredict the maximum lift, but the overall trend is consistent with the Mesh-A WMLES solutions and the experiment. For the post-stall cases, the WMLES lift predictions obtained on Mesh A are consistently closer to the experimental data than the predictions obtained on Mesh B.

Figure 13(b) shows the computed drag polars versus the lift coefficient and the corresponding experimental data. WMLES results on Mesh A and Mesh B closely follow the experimental drag-polar curve for lower angles of attack. At higher angles of attack, including $\alpha = 17.05°$ and $\alpha = 19.57°$, the WMLES computations on Mesh A continue to show good agreement with the experiment. In the post-stall regime, the lift-to-drag ratio obtained from both Mesh A and Mesh B is underpredicted. At $\alpha = 20.55°$, the drag discrepancy between WMLES and the experiment is approximately 1.8% for Mesh A and 1.3% for Mesh B. At $\alpha = 21.47°$, the drag deviation remains on the same level, about 1.4% and 1.5% for Mesh A and Mesh B, respectively.

Figure 13(c) shows the pitching-moment coefficients versus angle of attack. At all angles of attack except $\alpha = 21.47°$, the WMLES computations on Mesh A show good agreement with the experimental data. The maximum difference corresponding to $\alpha = 7.05°$ is about 4.6% and the minimum difference corresponding to $\alpha = 19.57°$ is within 1%. However, the magnitude of the pitching moment at the highest angle of attack, $\alpha = 21.47°$, is substantially underpredicted (i.e., pitching moment is not negative enough) on Mesh A as compared to the experimental data that indicates a strong nose-down pitching moment. The WMLES computations on Mesh B capture well the pitching-moment trend at all angles of attack, although at $\alpha = 19.57°$ and $\alpha = 20.55°$, the nose-down moment is slightly underpredicted compared to the experiment. An interesting observation is that the WMLES solution computed on Mesh B at $\alpha = 21.47°$ appears to indicate a stronger nose-down pitching moment than the WMLES solution computed on Mesh A. On Mesh B, the pitching moment at $\alpha = 21.47°$ is, in fact, slightly more negative than the moment at $\alpha = 20.55°$, which correctly reflects the increased nose-down tendency. Investigations are currently underway to understand if the differences observed at the highest angle of attack are caused by the grid resolution or cell topology. Uncertainties in the experimental data may also contribute to the discrepancies.

In Figs. 14–16, computed pressure distributions are compared with experimental data at three angles of attack. As mentioned previously, experimental data are available along each of the spanwise locations depicted in Fig. 9, although results are only shown for the stations indicated by the red lines to conserve space. Figure 14 shows pressure distributions
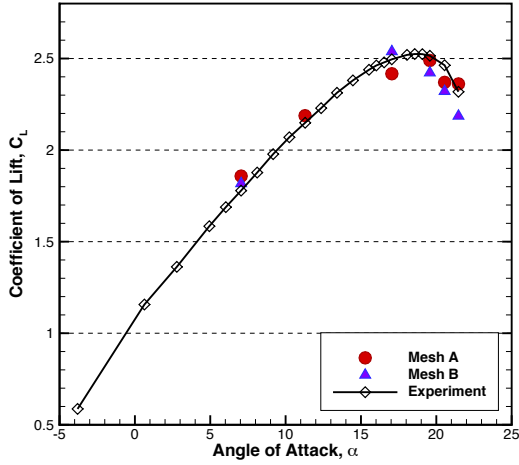
(a) Lift

(b) Drag

(c) Pitching moment
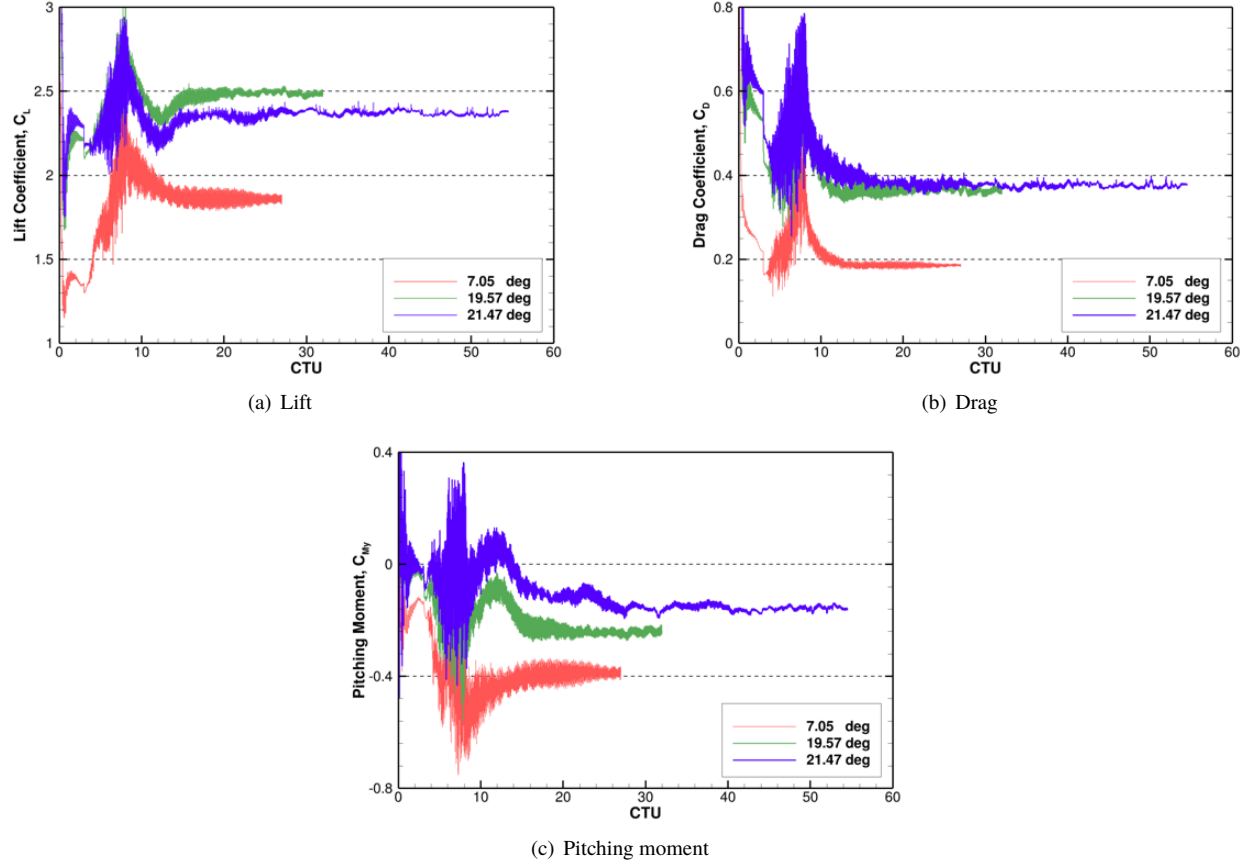
Fig. 12 Force and moment histories for NASA CRM-HL computations.

computed on Mesh A and Mesh B for α = 7.05°. At all spanwise stations, the computed pressure distributions are in good agreement with each other and the experimental data. Pressure distributions exhibit small oscillations on the slat at all spanwise stations, and on the flap at stations A, B, and C. Querying the skin friction indicates that these locations correspond to the flow transition from a smooth state to an oscillatory one. Longer time averaging is required to reliably assess the source of these oscillations.

Figures 15 and 16 show pressure distributions at α = 19.57° and α = 21.47°, respectively. At the most inboard spanwise location (Station A) at α = 19.57°, the pressure distributions on the flap computed on Mesh B achieve better agreement with the experiment than the pressure distributions computed on Mesh A. At all other spanwise stations, the pressure distributions computed on Mesh A and Mesh B are almost identical. The reasons for the differences at Station A are currently not known and more analysis is required. For this purpose, examining experimental data on the fuselage itself may be useful. Note that in Fig. 15, the pressure distributions computed on Mesh A show oscillations on the slat at the most inboard spanwise location, but the oscillations gradually lessen outboard. In contrast, the pressure distributions computed on Mesh B exhibit small oscillations at all the spanwise locations. Longer time-averaging may reduce, or even eliminate these oscillations as instantaneous pressure distributions (not shown) are extremely oscillatory in these regions.

At α = 21.47° shown in Fig. 16, noticeable differences between the computed pressure distributions and the experiment are observed on the slat at Station A. At Station A, the computed pressure distributions are also slightly different on the flap. On the slat, the pressure distributions computed on Mesh B have slightly less lift than the pressure distributions computed on Mesh A; on the flap, the pressure distributions computed on Mesh B have slightly more lift than the pressure distributions computed on Mesh A. Considering the slat and the flap together, these differences in lift indicate that Mesh B should have a greater "nose-down" pitching moment, which is reflected in Fig. 13.
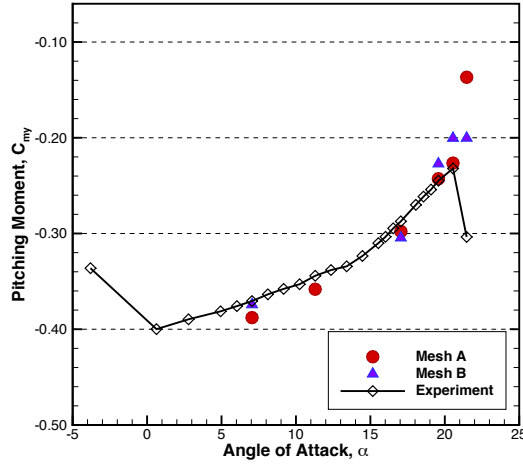
A third grid, Mesh C, has been generated to include a similar number of grid points as Mesh B, but with a larger normal spacing at the wall and uniform point distributions in the leading- and trailing-edge regions. While not a

15

(a) Lift vs. angle of attack
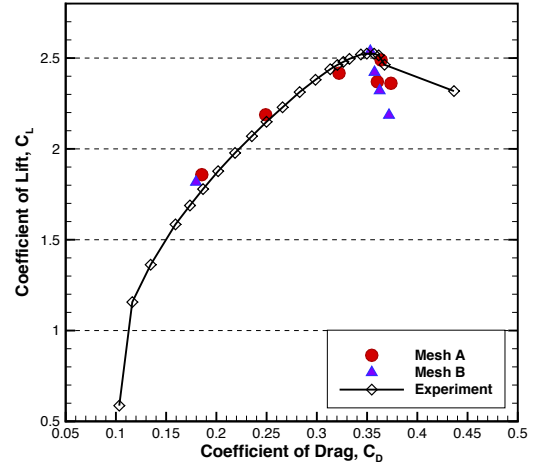
(b) Lift vs. drag

(c) Pitching moment vs. angle of attack

Fig. 13   Forces and moments for NASA CRM-HL.

rigorous comparison, this increase in wall-normal spacing has been imposed to examine whether a larger value of Δy_w^+ results in substantial changes in the flowfield. Because Mesh A contains the largest number of grid points among all the grids considered, pressure distributions computed on Mesh A are used as references. As representative comparisons, Figs. 17 and 18 show surface pressures computed on Mesh A and Mesh C for two angles of attack, namely $\alpha = 7.05°$ and $\alpha = 19.57°$, respectively, at Stations E and G. The pressure distributions indicate that larger value of Δy_w^+ leads to accuracy degradation. As shown in the Figs. 17 and 18, the pressure on the suction side is underpredicted at both stations for both angles of attack and for all wing components (slat, main wing, and flap). The underprediction becomes more severe from inboard to outboard. For reference, the pressure distributions computed on Mesh B (Figs. 14 and 15) show much better agreement with the experimental data. These observations emphasize the importance of proper Δy_w^+ (as well as grid clustering) in wall shear-stress modeling and highlight the effects on solution accuracy.

Instantaneous isosurfaces of Q-criterion computed on Mesh A are shown in Fig. 19 for the critical angle of attack of $\alpha = 19.57°$, near the maximum lift. Here, WMLES computations capture fine turbulent structures and propagate them downstream close to the wing/fuselage surface. Complicated vortical structures are observed near the the wing-root juncture region, the inboard slat, and the nacelle chine and nacelle/pylon. These geometrical features shed vortices and turbulent eddies that propagate to the wing inboard and fuselage areas. The vortices generated from the slat brackets

seem to be mild in strength as compared to other vortical systems.

To further visualize the basic structures of the flowfield, Figs. 20–22 show instantaneous contours of density-gradient magnitude computed on Mesh A for three angles of attack, namely $\alpha = 7.05°$, $\alpha = 19.57°$, and $\alpha = 21.47°$, at four stations, namely stations A, D, E, and G. At all the angles of attack, the slat wake is well captured and propagates across the main wing where it interacts with the turbulent boundary layer. At inboard and midspan stations, small-scale vortices are clearly observed. These vortices are generated from the trailing edge and the cove corner of the main wing, and carried all the way to the suction side of the flap. Similarly, vortex-shedding structures at the trailing edge of the flap in inboard and midspan stations can be clearly observed. Furthermore, for higher angles of attack, the interactions between the detached shear layer and turbulent boundary layer are strengthened to a large extent; more small-scales and turbulence features are captured in the boundary layer and wake areas.

Figure 23 depicts contours of the density-gradient magnitude computed on Mesh B at $\alpha = 21.47°$. Compared to the contours computed on Mesh A for the same angle of attack (cf. Fig. 22), the flow over the main element appears to be more separated, which may lead to lower lift values at the inboard sections.

Finally, contours of instantaneous skin-friction magnitude are shown in Fig. 24 for the $\alpha = 21.47°$ case on Mesh A and Mesh B. The WMLES computations on Mesh B appear to have slightly more inboard separation than the WMLES on Mesh A, although neither have massive separation. The slightly more separated flow computed on Mesh B is consistent with the stronger nose-down pitching moment shown in Fig. 13(c). Note that the outboard part of the wing does not show significant separation, which is commonly observed in RANS solutions and referred to as "pizza-slice" separation initiated by the slat bracket wakes.
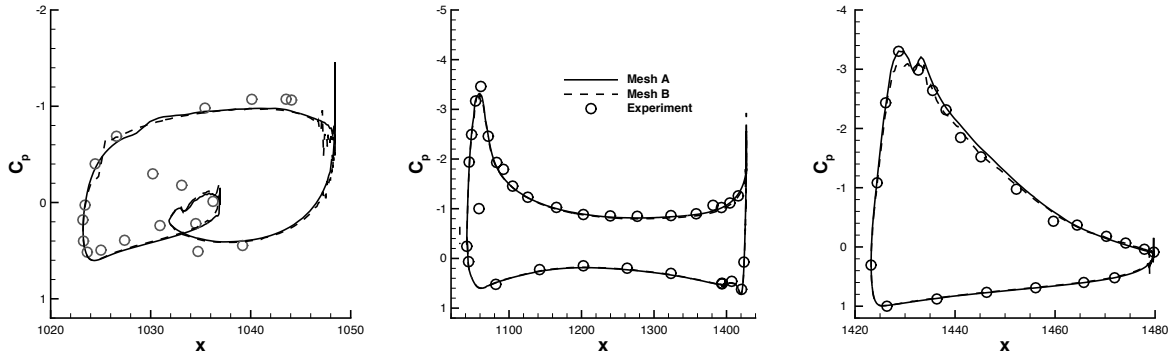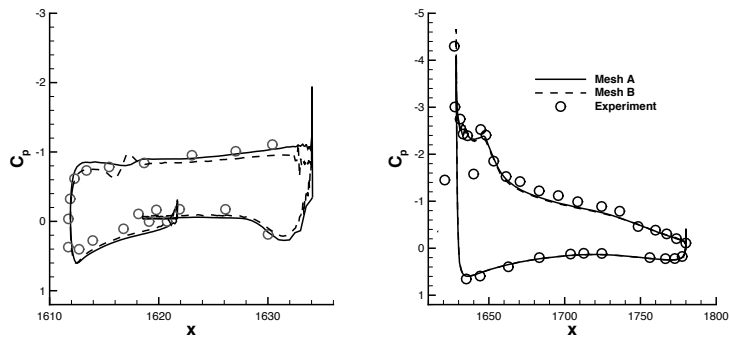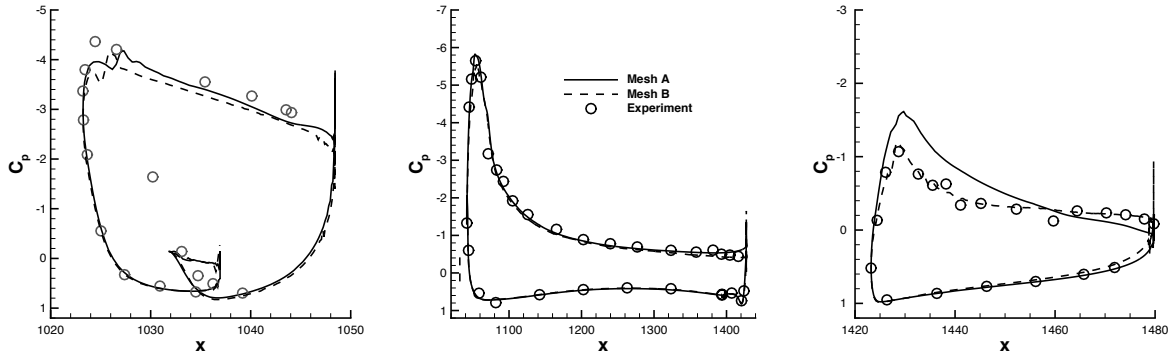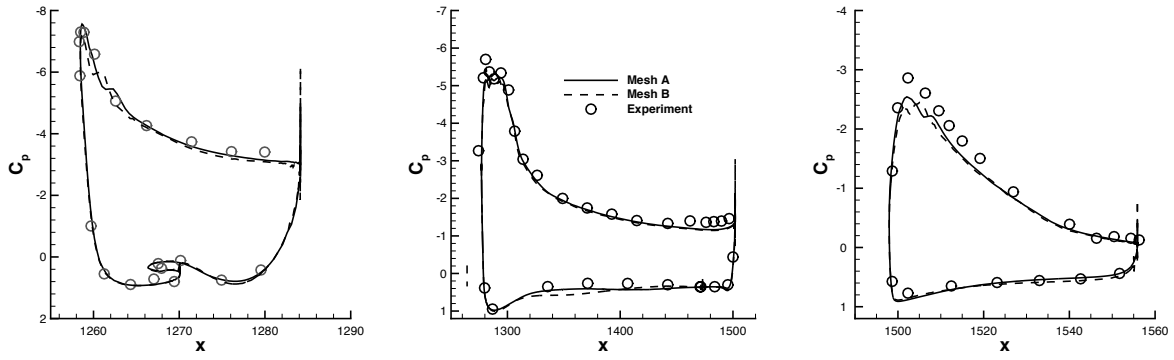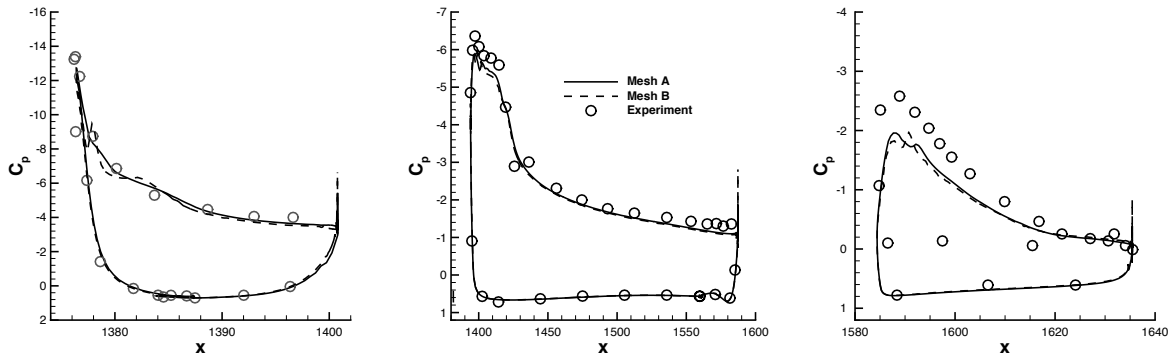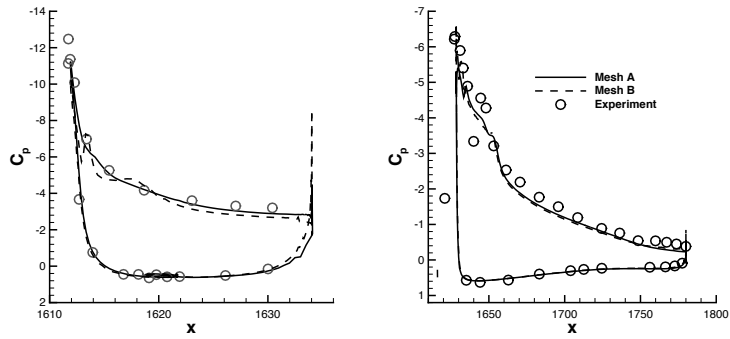
(a) Station A
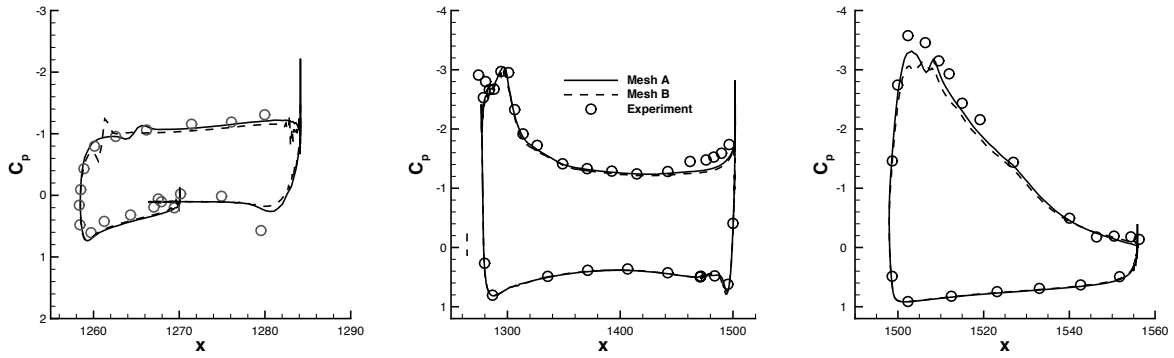
(b) Station D
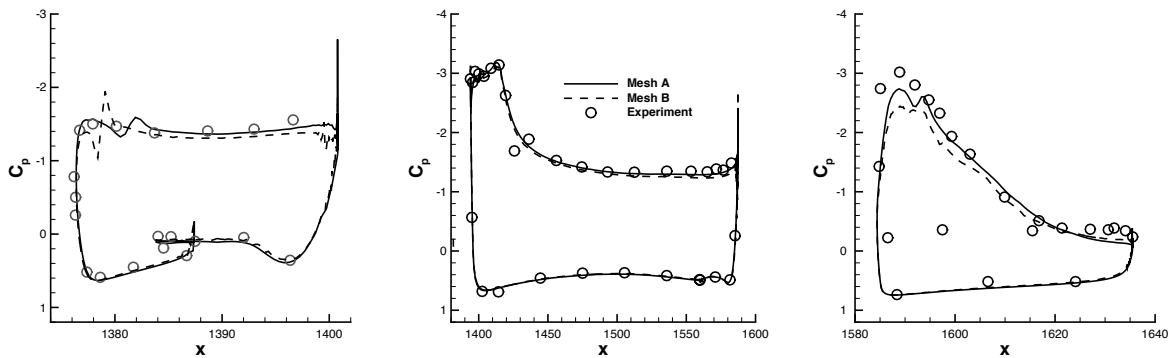
(c) Station E

(d) Station G

Fig. 14   NASA CRM-HL pressure distributions at four spanwise stations: $\alpha = 7.05°$.
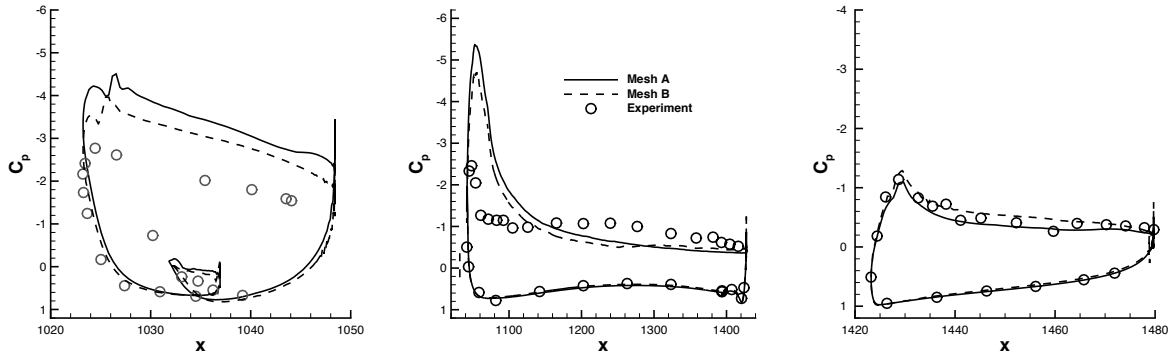
18

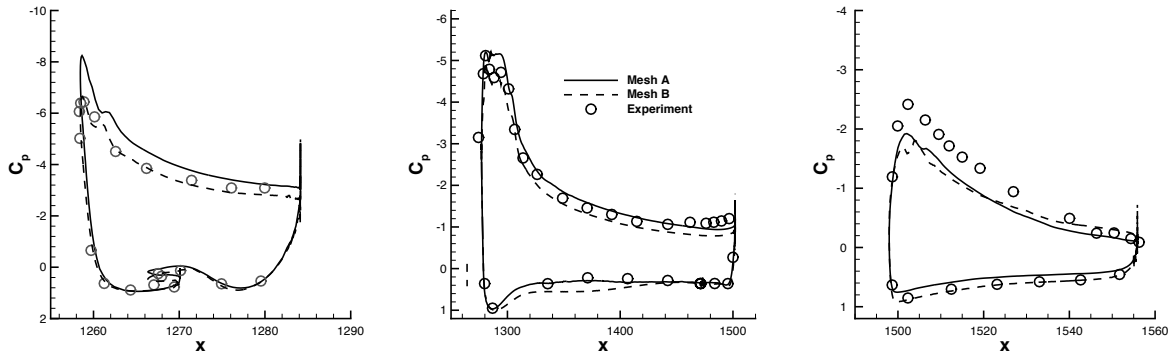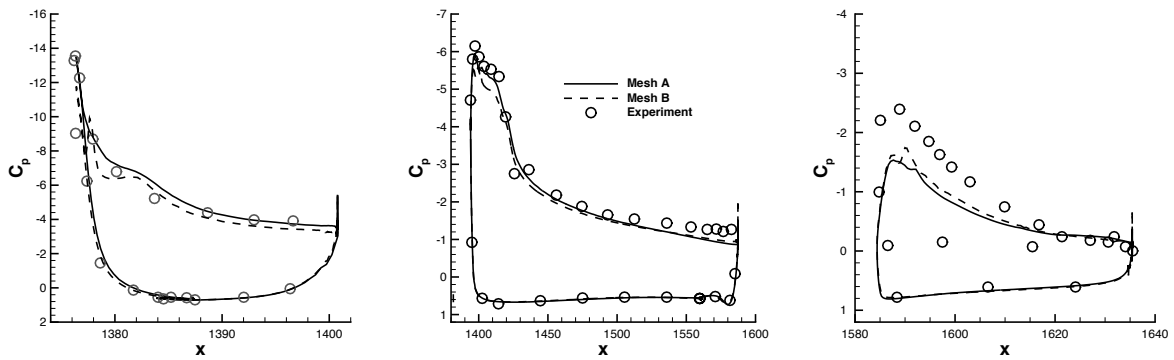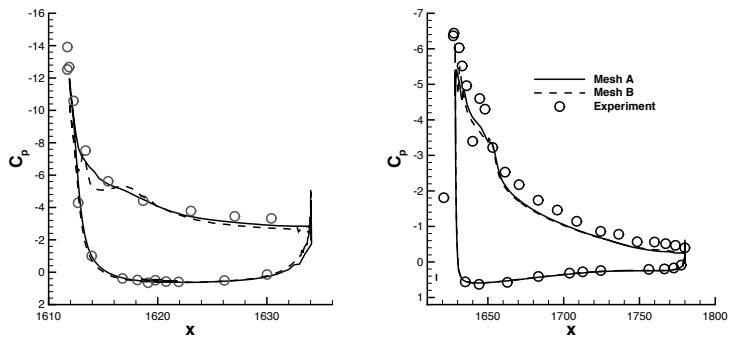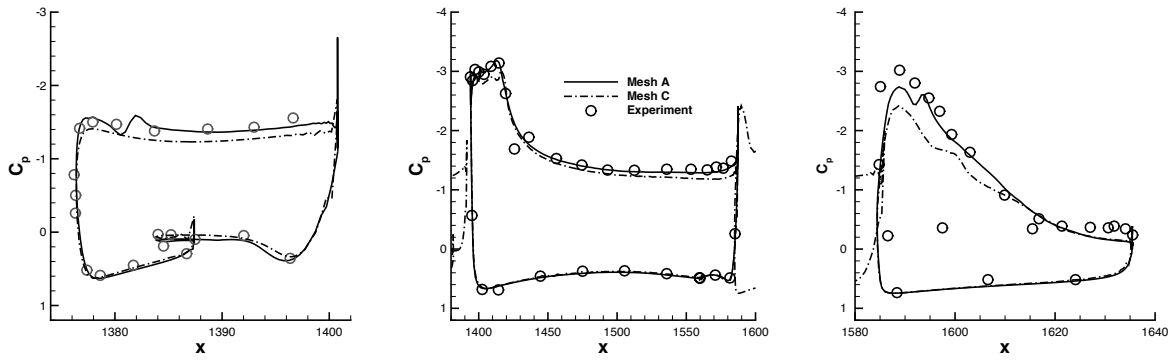(a) Station A

(b) Station D

(c) Station E

(d) Station G

Fig. 15 NASA CRM-HL pressure distributions at four spanwise stations: $\alpha = 19.57°$**.**

(a) Station A

(b) Station D

(c) Station E

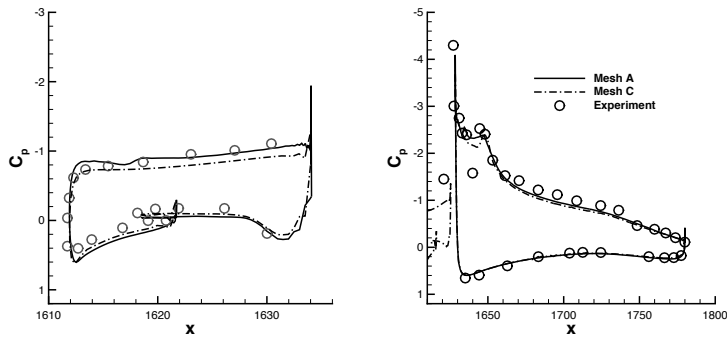(d) Station G

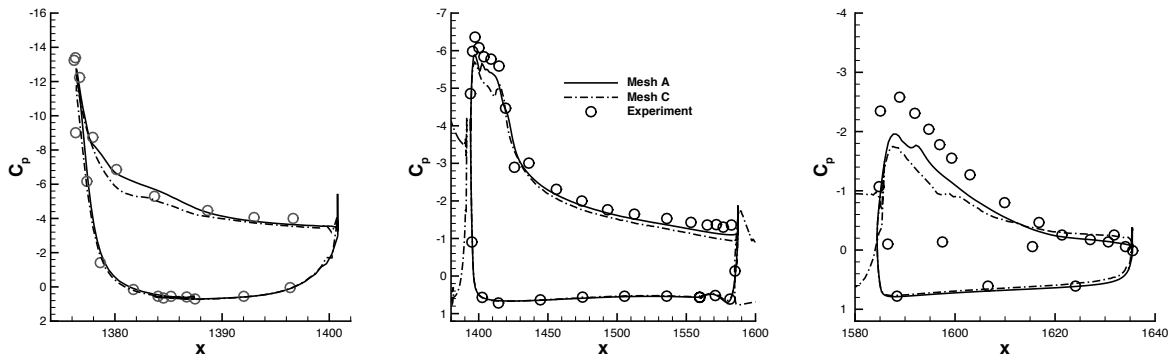**Fig. 16　NASA CRM-HL pressure distributions at four spanwise stations:** $\alpha = 21.47°$**.**
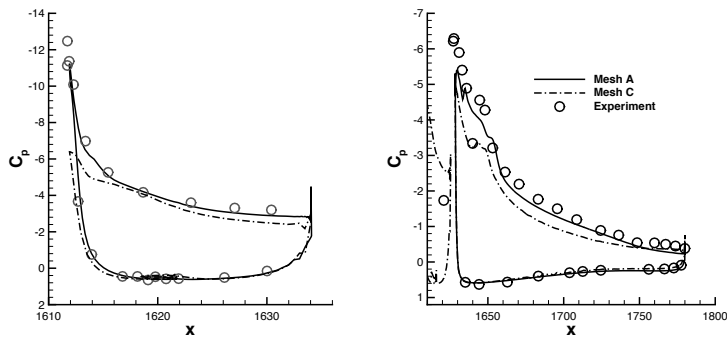
(a) Station E

(b) Station G

Fig. 17   NASA CRM-HL pressure distribution comparison between Mesh A and Mesh C: $\alpha = 7.05°$**.**

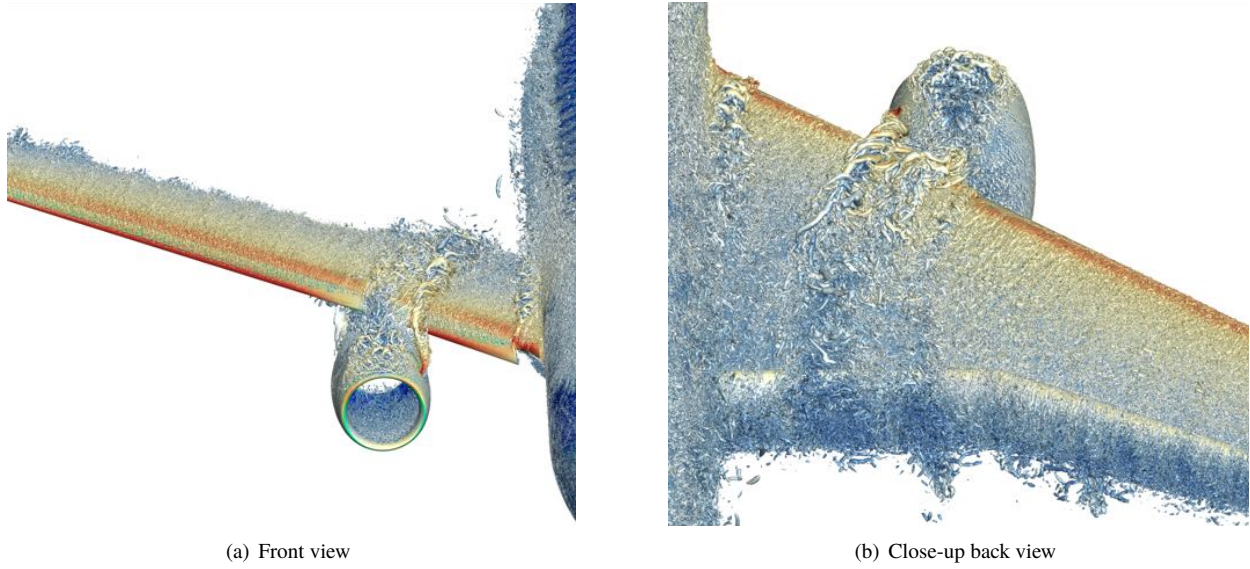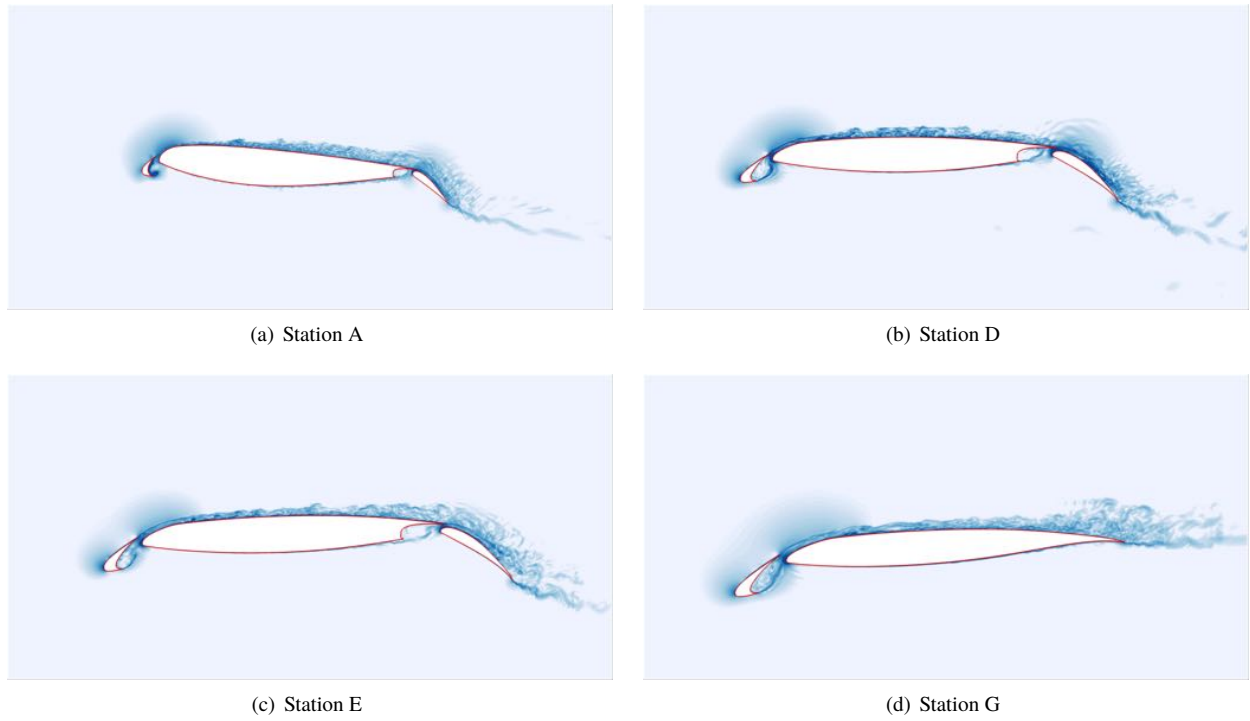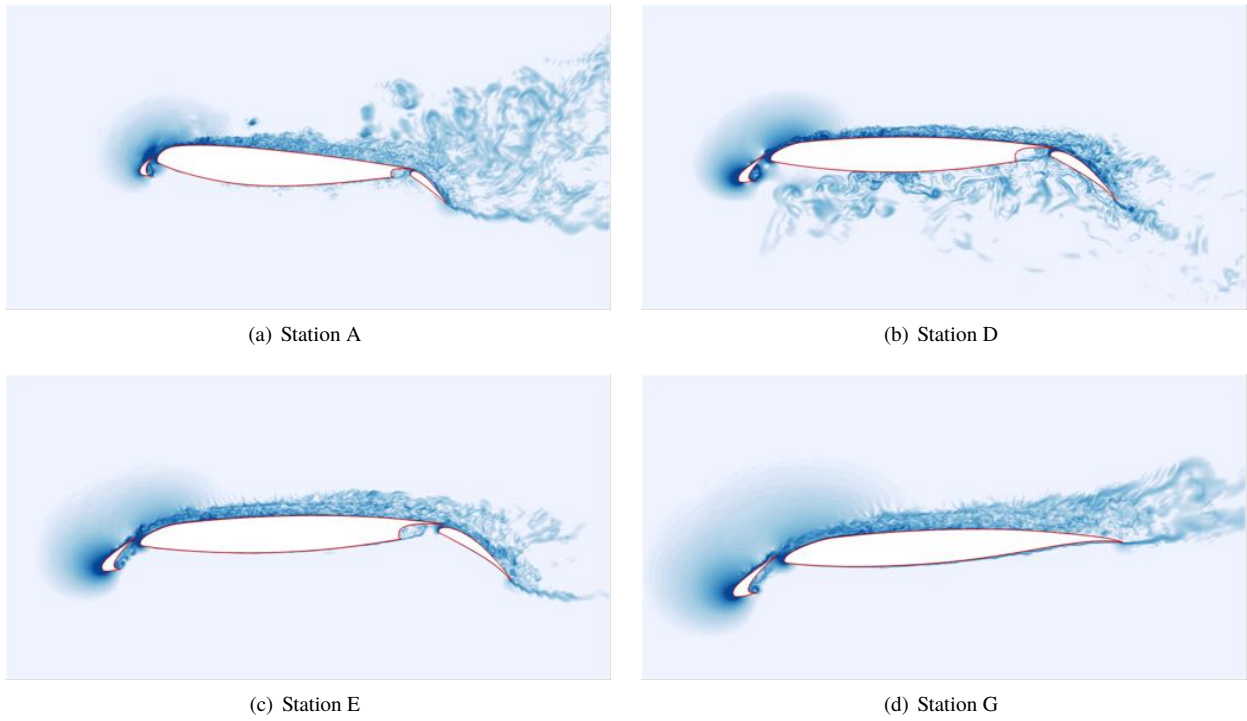
(a) Station E

(b) Station G

Fig. 18   NASA CRM-HL pressure distribution comparison between Mesh A and Mesh C: $\alpha = 19.57°$**.**

(a) Front view

(b) Close-up back view

Fig. 19   Instantaneous isosurfaces of Q-criterion over the NASA CRM-HL, colored by Mach number: $\alpha = 19.57°$**.**

(a) Station A

(b) Station D

(c) Station E

(d) Station G

Fig. 20   Magnitude of density-gradient for NASA CRM-HL at four spanwise stations on Mesh A: $\alpha = 7.05°$**.**

(a) Station A

(b) Station D

(c) Station E

(d) Station G

Fig. 21 Magnitude of density-gradient for NASA CRM-HL at four spanwise stations on Mesh A: $\alpha = 19.57°$**.**

(a) Station A

(b) Station D

(c) Station E
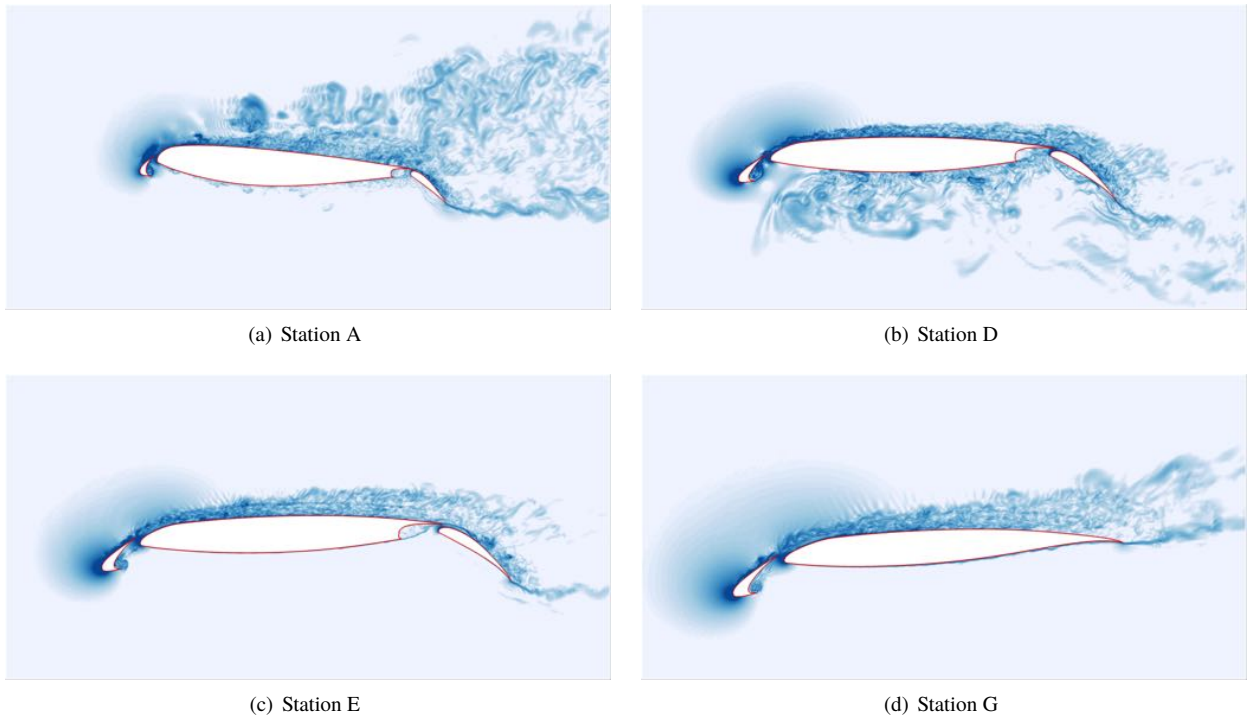
(d) Station G

Fig. 22 Magnitude of density-gradient for NASA CRM-HL at four spanwise stations on Mesh A: $\alpha = 21.47°$**.**

(a) Station A

(b) Station D

(c) Station E
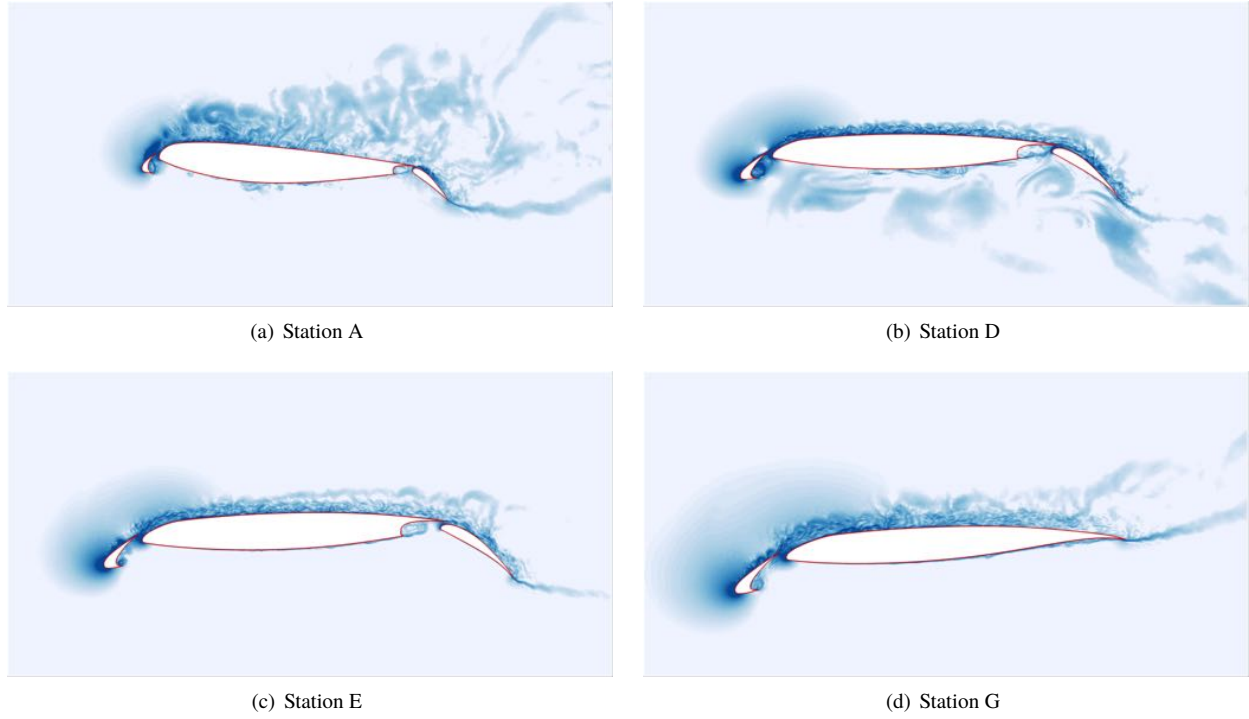
(d) Station G

Fig. 23   Magnitude of density-gradient for NASA CRM-HL at four spanwise stations on Mesh B: $\alpha = 21.47°$**.**

(a) Mesh A

(b) Mesh B
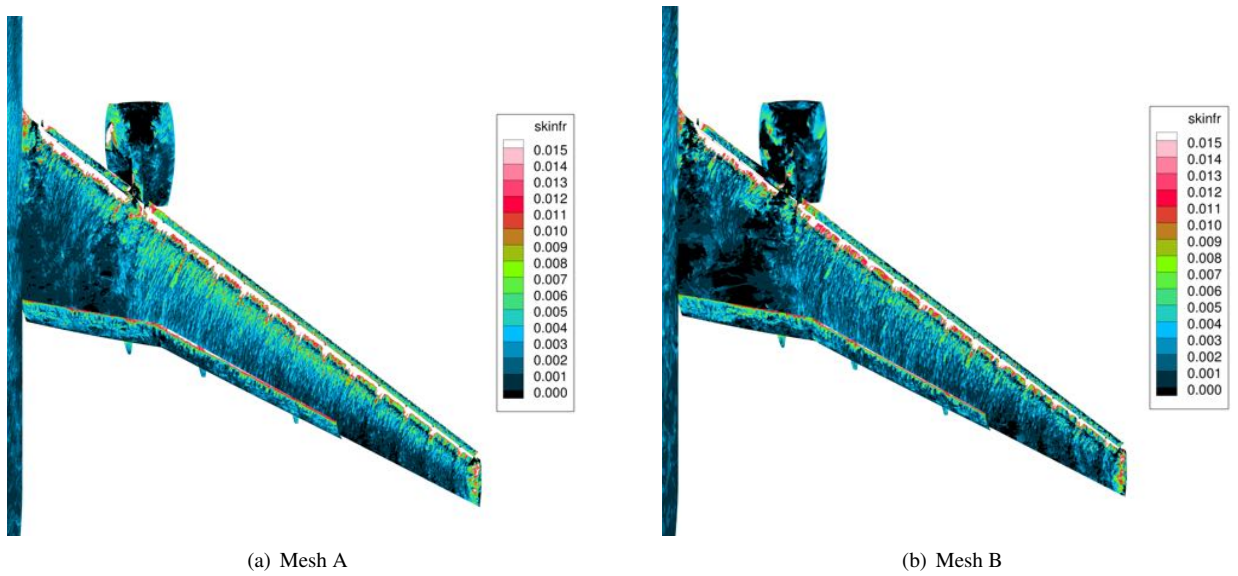
Fig. 24   Instantaneous skin friction for NASA CRM-HL: $\alpha = 21.47°$**.**

V. Conclusions

Wall-Modeled large-eddy simulation (WMLES) capability has been implemented in FUN3D, an unstructured-grid, finite-volume solver developed at the NASA Langley Research Center. The WMLES methodology has been evaluated for flows over a multielement 30P30N airfoil at various angles of attack. Good agreement has been established between the WMLES data and the experimental data for integrated forces, surface pressures, and boundary-layer velocity profiles. WMLES computations have also been performed for the NASA High-Lift Common Research Model. Free-air simulations have been systematically carried out using two grid systems containing approximately 418 million and 156 million grid points and a wide range of angles of attack covering the linear region of the lift curve, the maximum lift, and post-stall regimes. The integrated lift, drag, and pitching-moment quantities agree well with experimental measurements, although the computed pitching moment at the post-stall angle of attack of $\alpha = 21.47°$ does not show enough nose-down moment to exhibit a "pitch-break" phenomenon observed in the experiment. Distributions of surface pressure are compared with available experimental data, and good agreement is attained, including the critical angle of attack where maximum lift is observed experimentally.

Planned future work includes further investigations of post-stall flow conditions using enhanced mesh resolution to analyze the flow in the vicinity of the wing-root juncture. Future development efforts will include several approaches to improve solver performance as well as the application of mesh adaptation techniques for WMLES.

Acknowledgments

References

[1] Slotnick, J. P., and Mavriplis, D. J., "A Grand Challenge for the Advancement of Numerical Prediction of High-Lift Aerodynamics," AIAA Paper 2021–0955, 2021.

[2] Mauery, T., Alonso, J., Cary, A., Lee, V., Malecki, R., Mavriplis, D., Medic, G., Schaefer, J., and Slotnick, J., "A Guide for Aircraft Certification by Analysis," NASA CR-20210015404, NASA, May 2021.

[3] Rumsey, C. L., Slotnick, J. P., and Sclafani, A. J., "Overview and Summary of the Third AIAA High-Lift Prediction Workshop," *AIAA Journal*, Vol. 56, No. 2, 2019, pp. 621–644.

[4] Hinze, J. O., *Turbulence*, McGraw-Hill, 1975.

[5] Pope, S., *Turbulent Flows*, Cambridge University Press, 2000.

[6] Berselli, L., Iliescu, T., and Layton, W., *Mathematics of Large Eddy Simulation of Turbulent Flows*, Springer Science & Business Media, 2005.

[7] Sagaut, P., *Large Eddy Simulation for Incompressible Flows: An Introduction*, Springer Science & Business Media, 2006.

[8] Garnier, E., Adams, N., and Sagaut, P., *Large Eddy Simulation for Compressible Flows*, Springer Science & Business Media, 2009.

[9] Adams, N., and Hickel, S., "Implicit Large-Eddy Simulation: Theory and Application," *Advances in Turbulence XII*, 2009, pp. 743–750.

[10] Piomelli, U., and Balaras, E., "Wall-Layer Models for Large-Eddy Simulations," *Annual Review of Fluid Mechanics*, Vol. 34, No. 1, 2002, pp. 349–374.

[11] Spalart, P. R., "Detached-Eddy Simulation," *Annual Review of Fluid Mechanics*, Vol. 41, 2009, pp. 181–202.

[12] Fröhlich, J., and von Terzi, D., "Hybrid LES/RANS Methods for the Simulation of Turbulent Flows," *Progress in Aerospace Sciences*, Vol. 44, No. 5, 2008, pp. 349–377.

[13] Larsson, J., Kawai, S., Bodart, J., and Bermejo-Moreno, I., "Large Eddy Simulation with Modeled Wall-Stress: Recent Progress and Future Directions," *Mechanical Engineering Reviews*, Vol. 3, No. 1, 2016, pp. 15–00418.

[14] Kawai, S., and Larsson, J., "Wall-Modeling in Large Eddy Simulation: Length Scales, Grid Resolution, and Accuracy," *Physics of Fluids*, Vol. 24, No. 1, 2012, p. 015105.

[15] Kawai, S., and Larsson, J., "Dynamic Non-Equilibrium Wall-Modeling for Large Eddy Simulation at High Reynolds Numbers," *Physics of Fluids*, Vol. 25, No. 1, 2013, p. 015105.

[16] Park, G., "Wall-Modeled LES in Unstructured Grids: Application to the NASA Wall-Mounted Hump," AIAA Paper 2016–1560, 2016.

[17] Iyer, P. S., and Malik, M. R., "Wall-Modeled Large Eddy Simulation of Flow Over A Wall-Mounted Hump," AIAA Paper 2016–3186, 2016.

[18] Mettu, B. R., and Subbareddy, P. K., "Wall Modeled LES of Compressible Flows at Non-Equilibrium Conditions," AIAA Paper 2018–3405, 2018.

[19] Bodart, J., and Larsson, J., "Wall-Modeled Large Eddy Simulation of the McDonnell-Douglas 30P/30N High-Lift Airfoil in Near-Stall Conditions," AIAA Paper 2012–3022, 2012.

[20] Bodart, J., Larsson, J., and Moin, P., "Large Eddy Simulation of High-Lift Devices," AIAA Paper 2013–2724, 2013.

[21] Angelino, M., Fernandez-Yanez, P., Xia, H., and Page, G., "Large-Eddy Simulation with Modeled Wall Stress for Complex Aerodynamics and Stall Prediction," *AIAA Journal*, Vol. 59, No. 4, 2021, pp. 1225–1237.

[22] Lehmkuhl, O., Park, G., and Moin, P., "LES of flow Over the NASA Common Research Model with Near-Wall Modeling," Proceedings of the 2016 Summer Program, Center for Turbulence Research, Stanford University, 2016.

[23] Lehmkuhl, O., Park, G., Bose, S., and Moin, P., "Large-Eddy Simulation of Practical Aeronautical Flows at Stall Conditions," Proceedings of the 2016 Summer Program, Center for Turbulence Research, Stanford University, 2018.

[24] Goc, K. A., Moin, P., and Bose, S. T., "Wall-Modeled Large Eddy Simulation of An Aircraft in Landing Configuration," AIAA Paper 2020–3002, 2020.

[25] Valarezo, W. O., Dominik, C. J., McGhee, R. J., and Goodman, W. L., "High Reynolds Number Configuration Development of A High-Lift Airfoil," AGARD Meeting in High-Lift Aerodynamics, CP 515, 1992.

[26] Chin, V., Peters, D. W., Spaid, F. W., and McGhee, R. J., "Flowfield Measurements about A Multielement Airfoil at High Reynolds Numbers," AIAA Paper 93–3137, 1993.

[27] Evans, A. N., Lacy, D. S., Smith, I., and Rivers, M. B., "Test Summary of the NASA High-Lift Common Research Model Half-Span at QinetiQ 5-Metre Pressurized Low-Speed Wind Tunnel," AIAA Paper 2020–2770, 2020.

[28] White, F. M., and Corfield, I., *Viscous Fluid Flow*, Vol. 3, McGraw-Hill New York, 2006.

[29] Vreman, A. W., "An Eddy-Viscosity Subgrid-Scale Model for Turbulent Shear Flow: Algebraic Theory and Applications," *Physics of Fluids.*, Vol. 16, No. 10, 2004, pp. 3670–3681.

[30] Anderson, W. K., and Bonhaus, D. L., "An Implicit Upwind Algorithm for Computing Turbulent Flows on Unstructured Grids," *Computers & Fluids*, Vol. 23, No. 1, 1994, pp. 1–21.

[31] Biedron, R. T., Carlson, J.-R., Derlaga, J. M., Gnoffo, P. A., Hammond, D. P., Jones, W. T., Kleb, B., Lee-Rausch, E. M., Nielsen, E. J., Park, M. A., Rumsey, C., Thomas, J. L., Thompson, K. B., Walden, A. C., Wang, L., and Wood, W. A., "FUN3D Manual: 13.7," NASA/TM-0205010139, 2019.

[32] Roe, P. L., "Approximate Riemann Solvers, Parameter Vectors, and Difference Schemes," *Journal of Computational Physics*, Vol. 43, No. 2, 1981, pp. 357–372.

[33] Burg, C., "Higher Order Variable Extrapolation for Unstructured Finite Volume RANS Flow Solvers," AIAA Paper 2005–4999, 2005.

[34] van Leer, B., "Towards the Ultimate Conservative Difference Scheme, V. A Second Order Sequel to Godunov's Method," *Journal of Computational Physics*, Vol. 32, No. 1, 1979, pp. 101–136.

[35] Thomas, J. L., Diskin, B., and Nishikawa, H., "A Critical Study of Agglomerated Multigrid Methods for Diffusion on Highly-Stretched Grids," *Computers & Fluids*, Vol. 41, No. 1, 2011, pp. 82–93.

[36] Diskin, B., and Thomas, J. L., "Accuracy Analysis for Mixed-Element Finite-Volume Discretization Schemes," NIA Technical Report 2007-8, 2007.

[37] Thomas, J. L., Diskin, B., and Rumsey, C., "Towards Verification of Unstructured Grid Methods," *AIAA Journal*, Vol. 46, No. 12, 2008, pp. 3070–3079.

[38] Spalding, D. B., "A Single Formula for the "Law of the Wall"," *J. Appl. Mech.*, Vol. 28, No. 3, 1961, pp. 455–458.

[39] Carlson, J.-R., Vatsa, V. N., and White, J., "Validation of A Node-Centered Wall Function Model for the Unstructured Flow Code FUN3D," AIAA Paper 2015–2758, 2015.

[40] Nishikawa, H., "Beyond Interface Gradient: A General Principle for Constructing Diffusion Schemes," AIAA Paper 2020–5093, 2020.

[41] Vatsa, V. N., Carpenter, M. H., and Lockard, D. P., "Re-evaluation of An Optimized Second Order Backward Difference (BDF2OPT) Scheme for Unsteady Flow Applications," AIAA Paper 2010–0122, 2010.

[42] Wang, L., Diskin, B., Nielsen, E., and Liu, Y., "Improvements in Iterative Convergence of FUN3D Solutions," AIAA Paper 2021–0857, 2021.

[43] NASA and AIAA, "High-Lift Prediction Workshop," , Nov. 21, 2021 [Online]. URL https://hiliftpw.larc.nasa.gov/Workshop4/testcases.html.

[44] Klausmeyer, S. M., and Lin, J. C., "Comparative Results from A CFD Challenge Over a 2D Three-Element High-Lift Airfoil," NASA /TM-112858, 1997.

[45] Ducros, F., Ferrand, V., Nicoud, F., Weber, C., Darracq, D., Gacherieu, C., and Poinsot, T., "Large-Eddy Simulation of the Shock/Turbulence Interaction," *Journal of Computational Physics*, Vol. 152, No. 2, 1999, pp. 517–549.

[46] Rumsey, C. L., Lee-Rausch, E. M., and Watson, R. D., "Three-Dimensional Effects in Multielement High-Lift Computations," *Computers & Fluids*, Vol. 32, No. 5, 2003, pp. 631–657.

[47] Anderson, W. K., Bonhaus, D. L., McGhee, R. J., and Walker, B. S., "Navier-Stokes Computations and Experimental Comparisons for Multielement Airfoil Configurations," *Journal of Aircraft*, Vol. 32, No. 6, 1995, pp. 1246–1253.